Seasonal Variation of Saturn's Lyα Brightness

P Stephenson, T T Koskinen, Z Brown, Eric Quémerais, P Lavvas, J I Moses, B Sandel, R Yelle

The Astrophysical Journal, 971:89 (26pp), 2024 August 10 https://doi.org/10.3847/1538-4357/ad50a6

Seasonal Variation of Saturn's Lyα Brightness

P. Stephenson[1], T. T. Koskinen[1], Z. Brown[1], E. Quémerais[2], P. Lavvas[3], J. I. Moses[4], B. Sandel[1], and R. Yelle[1]
[1] Lunar and Planetary Laboratory, University of Arizona, Tucson, AZ, USA
[2] LATMOS/IPSL, Université de Versailles Saint-Quentin, Guyancourt, France
[3] GSMA, Université de Reims, Reims, France
[4] Space Science Institute, Boulder, CO, USA
Received 2024 February 7; revised 2024 May 16; accepted 2024 May 23; published 2024 August 7

Abstract

We examine Saturn's nonauroral (dayglow) emissions at Lyα observed by the Cassini/Ultraviolet Imaging Spectrograph (UVIS) instrument from 2003 until 2017, to constrain meridional and seasonal trends in the upper atmosphere. We separate viewing geometry effects from trends driven by atmospheric properties, by applying a multivariate regression to the observed emissions. The Lyα dayglow brightnesses depend on the incident solar flux, solar incidence angle, emission angle, and observed latitude. The emissions across latitudes and seasons show a strong dependence with solar incidence angle, typical of resonantly scattered solar flux and consistent with no internal source such as electroglow. We observe a bulge in Lyα brightnesses that shifts with the summer season from the southern to the northern hemisphere. We estimate atomic hydrogen optical depths above the methane homopause level for dayside disk observations (2004–2016) by comparing observed Lyα emissions to a radiative transfer model. We model emissions from resonantly scattered solar flux and a smaller but significant contribution by scattered photons from the interplanetary hydrogen (IPH) background. During the northern summer, inferred hydrogen optical depths steeply decrease with latitude toward the winter hemisphere from a northern hemisphere bulge, as predicted by a 2D seasonal photochemical model. The southern hemisphere mirrors this trend during its summer. However, inferred optical depths show substantially more temporal variation between 2004 and 2016 than predicted by the photochemical model. We benchmark our brightness values by comparing observed IPH Lyα emissions from Cassini/UVIS in 2006 with a model of the IPH emissions. Cassini/UVIS observations agree well with the modeled IPH background.

Unified Astronomy Thesaurus concepts: Planetary atmospheres (1244); Ultraviolet astronomy (1736); Upper atmosphere (1748); Atmospheric variability (2119); Saturn (1426)

1. Introduction

Lyα is the brightest ultraviolet emission line in the solar system and has been observed at Saturn since 1976, initially with sounding rockets and the Copernicus satellite (Weiser et al. 1977; Barker et al. 1980). Subsequent observations of Lyα emissions from Saturn were made by the Interplanetary Ultraviolet Explorer (Clarke et al. 1981; McGrath & Clarke 1992) and during the Voyager flybys with the Ultraviolet Spectrometer (UVS; Broadfoot et al. 1981; Sandel et al. 1982; Ben-Jaffel et al. 1995). Over its 13 yr mission, Cassini/Huygens (Matson et al. 2002) orbited Saturn, compiling an extensive data set of Lyα emissions with the Ultraviolet Imaging Spectrograph (UVIS; Esposito et al. 2005).

Recently, Ben-Jaffel et al. (2023) identified a bulge in Lyα emissions from Saturn's thermosphere in the northern hemisphere between latitudes of 5° and 35°N, with observations from the Hubble Space Telescope (HST) Space Telescope Imaging Spectrograph (STIS) and Cassini/UVIS. They also identified the same bulge in Voyager/UVS observations that probed Saturn's atmosphere close to the northern spring equinox 35 yr earlier (Yelle et al. 1986). They concluded that the observed northern hemisphere (NH) bulge is a permanent feature of the thermosphere. We note that this bulge shows no longitudinal variation and therefore differs significantly from the Lyα bulge that has been observed on Jupiter, which is fixed in system III longitude (Dessler et al. 1981; Skinner et al. 1988). Ben-Jaffel et al. (2023) proposed two primary mechanisms to drive the emission bulge: a variation of the temperature profile in the lower thermosphere and upper stratosphere or a previously unidentified suprathermal atomic hydrogen population at high altitudes, both of which could vary seasonally. They proposed that the suprathermal population could be created, for example, by a significant influx of material from the rings or Enceladus into the upper atmosphere. In this study, we examine Lyα emissions over the duration of the Cassini mission, in order to examine the cause of the bulge, whether it is a permanent feature of Saturn's thermosphere, and the source of the increased emissions.

At Lyα, Cassini/UVIS consistently observed much lower disk brightnesses compared to the observations of Voyager/UVS, with peak brightnesses of about 1 kR outside the auroral oval compared to 3–4 kR (1 Rayleigh $=10^6/4\pi$ photons cm^{-2} s^{-1} sr^{-1}[1]) during the Voyager flybys (Ben-Jaffel et al. 1995; Gustin et al. 2010; Shemansky et al. 2009; Koskinen et al. 2020). Gustin et al. (2010) suggested that the disparity was a result of ring-reflected light during the Voyager observations, while Shemansky et al. (2009) suggested strong electroglow emissions could reconcile the differences. The Voyager brightnesses have since been questioned and revised downward by Quémerais et al. (2013a), who concluded that the sensitivities of the Voyager/UVS instruments were underestimated by a factor of 1.5–2.5. The revised Voyager Lyα brightnesses are roughly consistent with those observed by Cassini/UVIS (Koskinen et al. 2020). Using HST observations

from an Earth orbit as a calibration standard, Ben-Jaffel et al. (2023) challenged the downward revision of the Voyager brightnesses and proposed instead a recalibration of the Cassini/UVIS instrument at Lyα that would increase the observed brightnesses by 80%. After scaling with the solar Lyα flux at different times, they compared several observations by Cassini/UVIS (in 2007, 2013, and 2014), HST/STIS (in 2017), and HST's Goddard High Resolution Spectrograph (in 1996) to arrive at this conclusion.

Cross-calibration of UV instruments between missions at Lyα remains difficult. Observations of Lyα emissions from interplanetary background hydrogen provide one method to facilitate it. Observations of the interplanetary hydrogen (IPH) Lyα by the Voyager/UVS instruments (Katushkina et al. 2016, 2017), New Horizons Alice (Gladstone et al. 2018, 2021) and future observations by PHEBUS on Bepi/Colombo (Quémerais et al. 2020), have and will continue to constrain models of the IPH background (e.g., Quémerais & Izmodenov 2002; Izmodenov et al. 2013; Quémerais et al. 2013a; Pryor et al. 2022). Models of the interaction between the local interstellar medium (LISM) and the solar wind (Quémerais et al. 2006; Izmodenov et al. 2001, 2013) are dependent on the hydrogen density of LISM and at the terminator shock near 90 au, with estimates of the LISM hydrogen density varying from 0.12 to 0.195 cm^{-3} (Dialynas et al. 2019; Swaczyna et al. 2020). In addition to scattered solar flux, a galactic contribution to the background of 40 R has been identified at large heliocentric distances (Gladstone et al. 2021; Pryor et al. 2022). While there remains uncertainty on the density of the LISM, we compare Cassini/UVIS Lyα observations to the model of Quémerais et al. (2013a) and find good agreement between Cassini/UVIS observed and modeled brightnesses, without the proposed recalibration by a factor of 1.7 (Ben-Jaffel et al. 2023; Pryor et al. 2024). Limb observations and solar occultations, in conjunction with photochemical models, can provide further constraints on the atomic hydrogen columns, Lyα emissions.

In addition to the Lyα bulge, Saturn's thermosphere also exhibits latitudinal variation in temperature (Brown et al. 2020) and exobase altitude that are likely to be seasonally variable (Koskinen et al. 2021). Stellar occultations by Cassini/UVIS have constrained the temperature of Saturn's thermosphere, allowing the retrieval of density profiles of upper atmospheric constituents, including H_2, He, and CH_4 (Shemansky & Liu 2012; Koskinen et al. 2013, 2015, 2016; Koskinen & Guerlet 2018; Brown et al. 2020, 2022). Stellar occultations are essentially self-calibrating and independent of instrument calibration. We note, however, that stellar occultations cannot be used to retrieve the density of H.

Latitudinal and seasonal trends in the upper atmosphere have been predicted by photochemical models (Moses & Bass 2000; Moses et al. 2000a; Moses & Greathouse 2005; Hue et al. 2015, 2016). This is because, for example, hydrocarbons in the stratosphere are influenced by meridionally varying insolation, including changes due to the motion of the ring shadow across Saturn's disk (Moses & Greathouse 2005). The variation of methane in the stratosphere also has a substantial impact on atomic hydrogen through both the production of H through photolysis (Moses et al. 2000a) and the location of the homopause. Comparison of photochemical models with Lyα observations from Cassini/UVIS can constrain the hydrogen column above the methane homopause, with methane as a strong absorber at Lyα. This can subsequently constrain eddy mixing and circulation near the homopause level (Atreya 1982, 1984 Sandel et al. 1982; Emerich et al. 1993; Moses et al. 2000a; Moses & Greathouse 2005).

The emissions of Lyα from Saturn's disk, observed by Cassini/UVIS, provide an extensive data set over 13 yr, with coverage across all latitudes. Koskinen et al. (2020) examined one observational sequence of Lyα from the Saturn disk in 2007. They found the brightnesses were consistent with resonance scattering of solar flux by a hydrogen column of 3×10^{16} cm^{-3}, in agreement with columns calculated with a photochemical model (Moses & Bass 2000; Moses et al. 2000b; Moses & Greathouse 2005). Several other case studies have been examined, particularly prior to 2008 (Mitchell et al. 2009; Shemansky et al. 2009; Gustin et al. 2010; Koskinen et al. 2020; Ben-Jaffel et al. 2023), but the full Lyα emission data set has not yet been fully explored.

By comparing results from a radiative transfer model with Cassini UVIS observations, we can estimate the effective optical depth of the atomic hydrogen layer. We follow the approach of Yelle et al. (1989) who modeled resonance scattering of a deep atmosphere by the iterative doubling and adding of thin layers, using angle-averaged partial frequency redistribution. We examine the variation of the effective hydrogen optical depths with latitude and season, under the assumption that emissions are dominated by resonant scattering by the ambient, thermal hydrogen population. In addition, we directly compare the inferred effective optical depths to the results of a seasonal photochemical model, to identify processes not included in the photochemical model, and to identify discrepancies that might indicate the presence of suprathermal atoms or internal emissions generated by photoelectron or energetic particle impact.

In this study, we examine the extensive data set of Lyα emissions from Saturn's dayside disk collected by Cassini UVIS from 2004 to the end of the mission in 2017. We consider the Lyα observations through three approaches, with the methods used outlined in Section 2. In Section 3.1, we compare observation of the IPH Lyα background to the model of Quémerais et al. (2013a). In Section 3.2, we employ a multivariate regresssion (MVR) analysis of the Lyα observations to confirm that resonance scattering of solar flux is the source of the emissions from Saturn's nonauroral, dayside disk. Finally, in Section 3.3, we compare the radiative transfer model, based on doubling and adding of thin layers, to the Lyα observations, and we retrieve the H optical depth above the methane homopause across the mission, to determine seasonal variation of Saturn's thermosphere. We discuss the results in Section 4, in particular with relation to the nature of the Lyα bulge. We also compare a seasonal photochemical model to the effective H optical depths retrieved in Section 3.3.

2. Methods

2.1. Cassini UVIS Data

We consider Cassini/UVIS observations from 2003 until 2017 during Cassini's orbits of Saturn, including MOSAIC, EUVFUV, and COMPSIT/the Cassini/Composite Infrared Spectrometer (CIRS) scans identified in the Planetary Data System. This first survey of the emission data focuses on nadir observations. Limb scans will not be considered in this work and are instead the subject of a future paper. The Cassini/UVIS

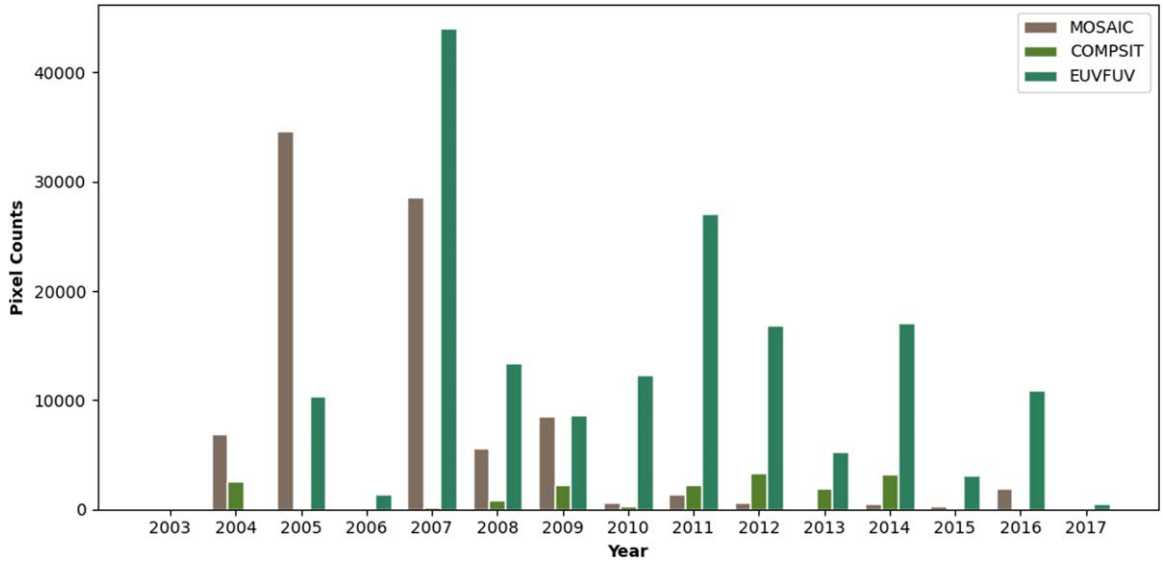

Figure 1. Number of observation pixels on Saturn's dayside disk, outside the auroral regions ($|\phi_{\rm lat}| < 65°$) by year and observation type (see text for an explanation of the types).

instrument comprised 64 spatial bins along the slit and 1024 spectral bins with a resolution of 0.78 Å. We focus on Lyα emissions from Saturn's disk using the far-UV (FUV) channel of UVIS (1115–1912 Å), integrating the emission brightness between 1205 and 1225 Å. We use the time-dependent sensitivity and flatfield updates that indicate a degradation of the signal by 30% from launch to the end of the mission, but in our default models, we do not use the proposed recalibration of the Cassini/UVIS instrument by a factor of 1.7 at Lyα (Ben-Jaffel et al. 2023, p24). While additional degradation at Lyα would not be surprising, cross-calibrating instruments with different viewing geometries and the use of IPH models for calibration also includes uncertainties. For example, our IPH model produces Lyα brightnesses consistent with UVIS observations without the additional calibration factor (see Section 3.1). The effective optical depths predicted by photochemical models of Saturn's atmosphere are also more consistent with UVIS observations with the previous calibration (see Section 3.3). In addition, we note that a calibration uncertainty of a factor of 2 does not affect our results with respect to both seasonal and meridional trends observed in the Lyα emission.

In order to reduce the downlink data volume and increase spatial coverage, the wavelength range of observations was sometimes reduced, and neighboring spectral pixels were combined (typically with a bin width of 4 pixels). In cases with no spectral binning, we use the Cube Generator from the Cassini/UVIS team and the pipeline flatfield to process the data. When spectral binning was applied, the pipeline flatfield does not appropriately address the presence of "evil" pixels on the detector, which returned much lower signals than those surrounding them. In the pipeline calibration, the intensity is interpolated to the "evil" pixels, which are assigned the value NaN in the flatfield. With binned spectra, one evil pixel in the bin results in a NaN value for the whole bin, losing information from the adjacent pixels. In these cases, we process the data with the Cube Generator with no flatfield, applying the derived 2007 flatfield correction of Koskinen et al. (2020) for binned data. The only observations that use spectral binning occur between 2004 and 2008, and we do not expect a substantial change in the flatfield correction over this period.

The three observation classes (MOSAIC, EUVFUV, and COMPSIT/CIRS) had different aims and characteristics. MOSAIC observations were designed to maximize spatial coverage, observing much or all of the Saturn system (including the rings). Prior to 2008, spectral binning of width 4 was common allowing integration times of 25–95 s. After 2008, the MOSAIC observations did not use any spectral binning and required longer integration times from 120 to 900 s. During EUVFUV observations, spectra from both the EUV and FUV channels were retrieved, with no spectral binning. These often capture a substantial part of the Saturn system using an integration time between 180 and 260 s. Finally, the COMPSIT/CIRS observations were paired with observations by CIRS (Flasar et al. 2005). These do not use any spectral binning and have much smaller spatial coverage, often only observing along a single line across Saturn's disk and limb. However, the long integration times (1200 or 2400 s) provide excellent signal-to-noise ratios for the spectra.

The UVIS data set comprises 636 observations over 14 yr comprising 140,925 scans and 8,032,725 pixels, of which 3,000,000 are on the dayside of Saturn's disk. In this study, we focus on airglow emissions and therefore exclude the auroral regions with latitudes poleward of 60°. Figure 1 shows the number of observation pixels by observation type and year. Additionally, over large periods, much of Saturn's disk was shadowed by the Saturnian rings. We do not have a good constraint on the solar flux entering the atmosphere after absorption in the ring atmosphere, so these points are removed from the data set. For each observation, the ring shadow region and rings are mapped onto the surface of Saturn (e.g., see Figure 2).

2.2. Multivariate Quadratic Regression of UVIS Data

In this section, we outline a data based approach to the analysis of the Lyα emissions from Saturn, which is independent of radiative transfer (RT) modeling. This helps to identify the key emission source of Lyα at Saturn and to test the assumptions used in the RT model. For this purpose, we

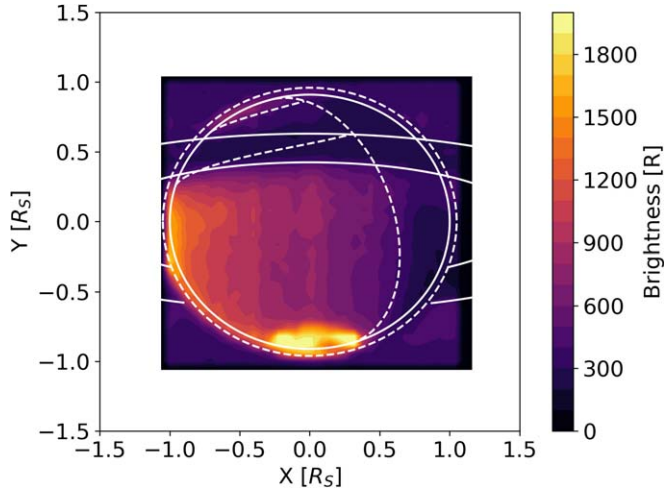

Figure 2. Observed Lyα emission brightness from Saturn on 2005 Jun 21. The solid white lines outline Saturn's disk and its rings. Dashed lines show the ring shadow region (at this time in the northern hemisphere), the terminator, and the position of the exobase.

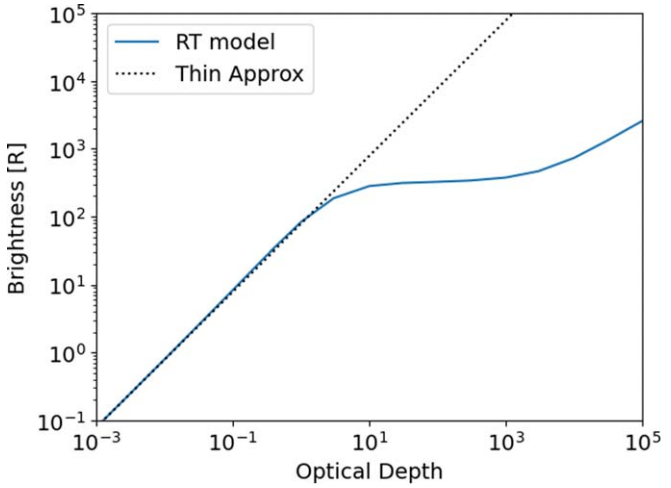

Figure 3. (Blue) Brightness vs. optical depth for resonance scattering of Lyα by atomic hydrogen for $(\theta_{in}, \theta_{em}) = (0, 0)$. The optically thin approximation is given by the black dotted line.

consider emission observations from 2014 until the end of the mission, from MOSAIC, EUVFUV, and COMPSIT/CIRS observations. We primarily focus on part of the northern hemisphere summer (2014–2017), such that the meridional trends in the atmosphere and emissions do not change substantially with time.

We use a multivariate regression with independent variables of emission angle, incidence angle, and latitude, which are used to predict the observed Lyα brightness. For simplicity, we have removed the dependence on the solar flux variation by scaling all the brightnesses to the solar flux applicable on 2016 Jan 1 (see Section 2.3.1). We choose these variables because resonance scattering is strongly dependent on the solar incidence angle and the emission angle of the observation, and because previous studies have identified meridional trends in the Lyα emissions. The model includes a quadratic in emission and incidence angles, in addition to a cubic in latitude. The full expression used for the regression is

$$B = p_0 + p_1 \cdot \theta_{em} + p_2 \cdot \theta_{in} + p_3 \cdot \phi_{lat} + p_4 \cdot \theta_{em}^2 + p_5 \cdot \theta_{em} \cdot \theta_{in} + p_6 \cdot \theta_{in}^2 + p_7 \cdot \phi_{lat}^2 + p_8 \cdot \phi_{lat}^3, \quad (1)$$

with p_i the coefficients, θ_{em} is the emission angle, θ_{in} is the solar incidence angle, and ϕ_{lat} is the planetocentric latitude. We prepare the data by standardizing the independent variables (θ_{em}, θ_{in}, ϕ_{lat}), and then transforming them into the required polynomial expressions in Equation (1). The 86,913 pixels in the NH summer were randomly split by 80%–20% into training and testing sets, respectively. The model was then trained using a least-squares regression. Monte Carlo analysis was used to retrieve confidence intervals for the coefficients, resampling the data set 1000 times.

2.3. Radiative Transfer Modeling

In order to constrain the properties of the atmosphere, we model the brightness of scattered solar and IPH Lyα using a radiative transfer model based on doubling and adding, which includes an angular dependent frequency redistribution function (Yelle 1988; Wallace et al. 1989; Yelle & Wallace 1989). The model is based on assumptions of a plane-parallel and isothermal atmosphere. The plane-parallel assumption breaks down for observations close to either the limb or the terminator, as the incidence or emission angles near 90°. Consequently, we only apply the model to cases of $\theta_{em} < 60°$ and $\theta_{in} < 65°$. Thin layer approximations of scattering and transmission functions (outlined in Appendix B; Yelle 1988) are iteratively doubled in thickness (see Appendix A), computing new scattering, transmission, and extinction functions until the required optical depth is reached.

The scattering and transmission functions are dependent on the atmospheric temperature (via the Lyα lineshape in the thermosphere) and the optical depth. We use a thermospheric temperature that varies with latitude, based on the pole-to-pole map of stellar occultations of Cassini/UVIS throughout 2017 (see Section 2.3.3; Brown et al. 2020). Figure 3 shows the variation in brightness as the atomic H optical depth increases, for the nadir case $(\theta_{in}, \theta_{em}) = (0, 0)$. The approximation for an optically thin atmosphere is given by the dotted line. The RT model is identical to the optically thin approximation at small optical depths, before deviating as it approaches $\tau = 1$. Beyond this, the atmosphere is optically thick, and the output brightness varies little as the column grows. At $\tau = 10^3$, the brightness then begins to increase once again, as frequency redistribution becomes more effective, and photons in the Lorentzian wings begin to undergo multiple scattering. For deep atmospheres, like Saturn's, the frequency redistribution is critical to computing the scattered brightness, due to the scattering of photons initially far from the line center.

2.3.1. Scattered Solar Flux

For scattered solar flux, the brightness of Lyα is dependent on the magnitude and shape of the solar flux entering the top of the atmosphere. The RT code is normalized to the solar flux at line center. For the magnitude of the flux, we use the LISIRD composite Lyα database (Machol et al. 2019), which is based on fluxes measured at 1 au by various instruments (e.g., Hinteregger et al. 1981; Barth et al. 1983; Woods et al. 2000; McClintock et al. 2005). First, we correct the LISIRD date for the flux to match the solar longitude at Saturn during the UVIS observation, which requires a shift of up to 15 days depending on the relative positions of Earth and Saturn. This is converted

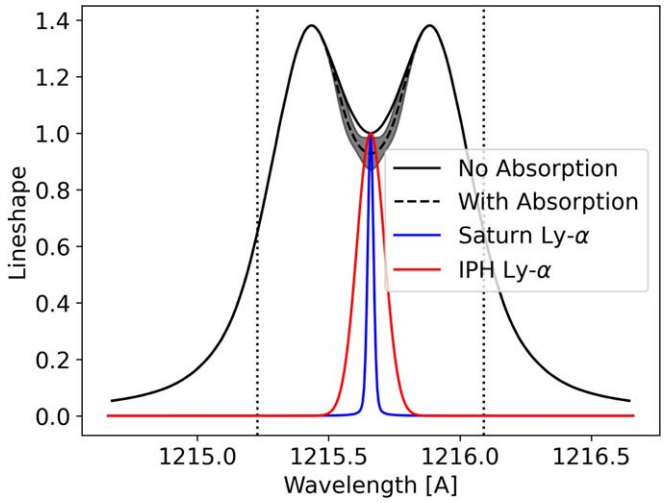

Figure 4. (Black solid line) Lineshape of the solar Lyα flux (black) at 1 au normalized to 1 at the line center. (Black dashed line and shaded region) Lineshape of solar Lyα after absorption of solar flux by the IPH background. (Blue) The Voigt profile of Lyα in Saturn's thermosphere for a temperature of 350 K. (Red) The lineshape of the IPH Lyα entering the upper atmosphere at $T_{\rm IPH} = 10{,}000$ K. The dotted vertical lines show the integration limits of $\pm 44 \Delta\nu_{D,\rm Sat}$, used in the radiative transfer model.

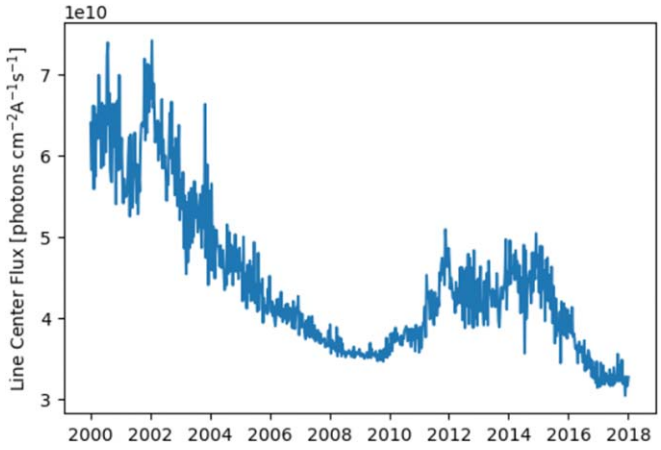

Figure 5. Lyα flux at Saturn throughout the Cassini mission, extrapolated from LISIRD fluxes at 1 au. This does not include absorption of the solar flux between 1 au and Saturn, which is accounted for separately.

to a line center flux using the line shape from Lemaire et al. (2005), imposed at 1 au (see Figure 4). After this, we extrapolate the flux to Saturn using an inverse square law with heliocentric distance (see Figure 5). We include absorption of the solar flux between 1 au and Saturn by the IPH background, using the IPH model described in Section 2.3.2. Once normalized, the modeled brightness based on scattered solar flux from Saturn's atmosphere is interpolated to the emission and solar incidence angle of a given observation, giving brightness as a function of temperature, effective H column optical depth, and viewing geometry. The temperature is constrained by a fit with latitude to the results retrieved from stellar occultations of the thermosphere (see Section 2.3.3).

2.3.2. Lyα from the Interplanetary Background

Lyα flux emitted by the IPH background is also scattered by Saturn's upper atmosphere. Unlike the solar flux, the IPH Lyα radiation covers the sky, so we integrate the IPH flux that enters from all directions (see Appendix C for further details). The flux entering the atmosphere from each direction is calculated with an IPH background model of Quémerais et al. (2013a). This model incorporates an angular dependent partial frequency redistribution to treat the resonant scattering of solar Lyα radiation by IPH distribution (Quémerais 2000; Quémerais et al. 2003). The distribution is calculated from the interaction of LISM with the solar wind (Izmodenov et al. 2001, 2013), using a hydrogen density of $n_{\rm H,TS} = 0.09\,{\rm cm}^{-3}$ and $n_{\rm H} = 0.14\,{\rm cm}^{-3}$ in LISM (Bzowski et al. 2009; Izmodenov & Alexashov 2020). We do not include an additional contribution of a 40 R galactic contribution (Gladstone et al. 2021; Pryor et al. 2022) that is isotropic. However, at distances of 9–10 au, the galactic contribution is small in comparison to IPH-scattered solar flux. The brightness, line width, and temperature of the IPH Lyα is calculated by integrating the emissions along the line of sight.

The brightness of the IPH emission line varies strongly with direction of observation, being largest close to the sunward direction when at large heliocentric distances. The position of the observer relative to the flow of LISM also impacts the variation of Lyα with the line of sight, although to a lesser extent. Here, we consider two positions in the IPH: the position of Saturn in 2006 and 2016. In both cases, we construct a full sky map of the Lyα brightness at the position of Saturn (e.g., Figure 6(a)). The IPH Lyα brightness can be parameterized as a function of the angle to the direction of maximum brightness ($\theta_{\rm Max}$, Figure 6(b)). We fit this as a sum of a quadratic and an exponential with respect to $\cos\theta_{\rm max}$. At heliocentric distances of 10 au, the maximum in the IPH density and Lyα brightness are closely aligned with the sunward direction.

2.3.3. Hydrogen Effective Optical Depths

The radiative transfer model combining scattering of solar and IPH Lyα photons is used to calculate the brightness as a function of the optical depth of the effective H column in the atmosphere, emission and incidence angle, and atmospheric temperature $B_{\rm RT}(\tau_{\rm H}, \theta_{\rm em}, \theta_{\rm in}, T_{\rm Sat})$. By effective optical depth, we refer to the vertical Lyα line center optical depth of the H column above the methane homopause. It is important to note that we assume all light at Lyα to be absorbed below the homopause. We do not self-consistently simulate absorption by CH_4 because seasonal changes to the depth of the homopause are not known a priori. This effort represents the first, zeroth-order effort to constrain variations in the effective H scattering column in the thermosphere. We have therefore chosen to follow this simplified, retrieval-type approach in our modeling.

We use a variable temperature profile with latitude, based on stellar occultations by UVIS (Brown et al. 2020) combined with CIRS limb scans (Guerlet et al. 2018; Koskinen & Guerlet 2018; Brown et al. 2024). Thermal structure is also expected to be seasonally variable, but the general characteristics of the temperature distribution, including the gradient between the auroral regions and the equator, are relatively stable, even on multidecadal timescales (Koskinen et al. 2021). We calculate the pressure-averaged temperatures ($\bar{T}_P = 1/[\ln(p_1/p_0)] \int_{P_0}^{P_1} T\,(d\ln P)$) above the methane homopause, which are then fit with a sixth-order polynomial (red, Figure 7). Here, the CH_4 homopause is defined as the location where $\tau_{\rm CH_4} = 1$ at Lyα in the atmospheric structure models fitted to the occultations and CIRS observations (e.g., Koskinen & Guerlet 2018; Brown et al. 2024). As noted above, the homopause location is obviously expected to change over time, but

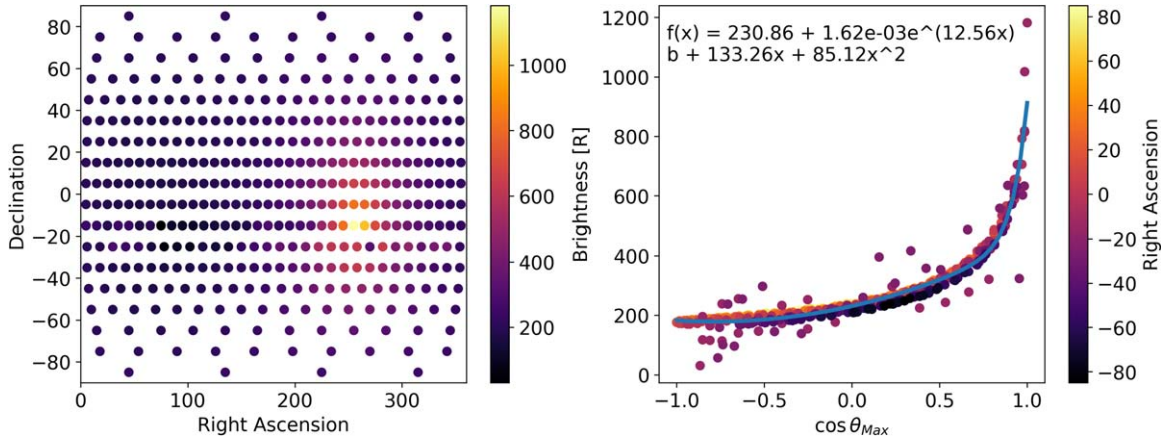

Figure 6. (Left) Full sky map of IPH brightness at Saturn in 2016, modeled as described in Section 2.3.2. (Right) Modeled IPH Lyα brightness against angle to direction of maximum brightness. The fit to the IPH brightness is shown in blue.

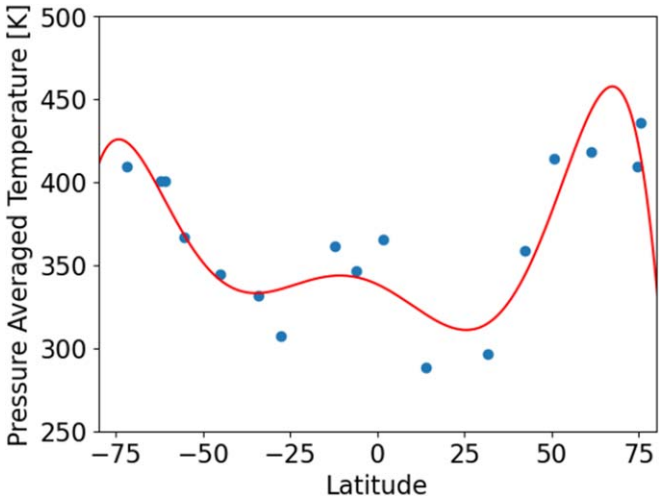

Figure 7. (Blue) Pressure-averaged temperatures above the methane homopause, from a 1D photochemical model (see Section 2.4), constrained by stellar UVIS occultations throughout 2017 (Brown et al. 2020). (Red) The temperatures are fitted with a sixth-order polynomial.

the pressure-averaged temperatures are nevertheless assumed to remain relatively stable. The polynomial fit is used to convert the latitude of observation into an atmospheric temperature in the radiative transfer model.

For each pixel, characterized by incidence angle, emission angle, and latitude (temperature), the brightness against optical depth is interpolated to the viewing geometry. Using this monotonic relationship, the observed Lyα brightness for each pixel is converted to an effective hydrogen optical depth for each pixel (Figure 8). We use Monte Carlo error estimation, allowing for uncertainty in the Lyα brightness from the UVIS instrument, as well as uncertainty in the solar flux normalization and absorption of the solar flux between the Sun and Saturn.

2.3.4. Other Sources of Lyα

In comparing the radiative transfer model with the observed brightnesses, we ignore the possibility of internal sources and scattering by suprathermal atomic H. However, we considered the following potential emission sources that are likely to be insignificant:

1. photoelectron impact excitation;
2. H^+ recombination;
3. scattering by hot hydrogen in the thermosphere, produced via H_3^+ recombination.

Waite et al. (1983) used a two-stream model to examine Lyα emissions driven by photoelectrons at Jupiter, finding a total contribution of 26 R. Extrapolating this to Saturn, we expect a factor of 3–4 reduction in the photoelectrons based on the reduced solar flux at Saturn, and the emitting column of H at Saturn is approximately a factor of 3 smaller than at Jupiter. Therefore, we expect photoelectron-induced Lyα emissions to be negligible compared to scattered solar flux.

Recombination is a well-known astrophysical source of Lyα emissions, and a possible source in hot exoplanet atmospheres. In cold planetary atmospheres, however, it is negligible. For H^+ recombination, we calculate the case-B recombination rate using H^+ and e^- profiles from the 1D photochemical model (Moses et al. 2023), to estimate an upper limit for the production of excited H atoms ($n \geqslant 2$). Integrating this over the atmospheric column gives a column emission of only $\sim 10^{-3}$ R.

One source of hot hydrogen in the upper atmosphere is the recombination of H_3^+, producing $H + H + H$ and $H + H_2$. We constrain this source by using the photochemical model profiles (Moses et al. 2023). At the zeroth order, we assume a local production of hot H (rates listed in Larsson et al. 2008) balanced by local cooling through elastic collisions of the hot H with thermal H and H_2, with collision cross sections from Krstić & Schultz (1999). Under this assumption, the hot H population generated by the recombination of H_3^+ in the upper atmosphere is negligible, with column densities a factor of 10^7 smaller than the ambient atomic hydrogen column density. This hot H population is too small to generate Lyα emissions comparable to the scattering by the thermal H population (a column of hot atoms a factor of 10^4 smaller than thermal H could generate similar emissions).

H_3^+ rain from the rings has been observed at Saturn (O'Donoghue et al. 2019). However, the ring rain latitudes show no obvious correlation with the observed Lyα bulge, and it is difficult to anticipate a related mechanism that could generate enough hot atoms to explain the bulge. While we cannot rule out a hot population generated by another means, the observations and modeling at present appear most consistent with emissions

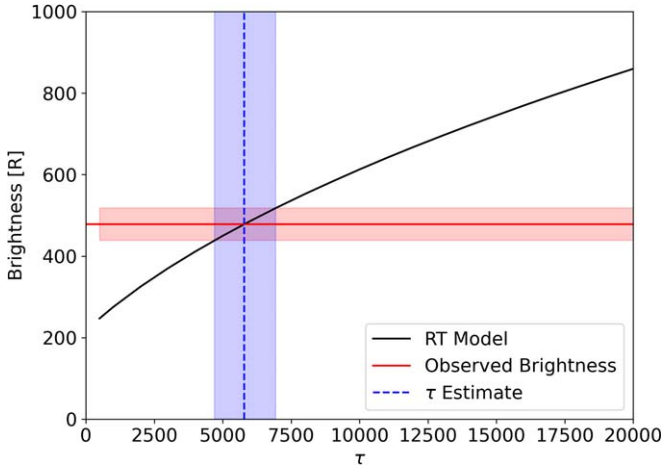

Figure 8. Retrieval of optical depth estimates (blue) by comparison of Cassini/UVIS observations (red) with the radiative transfer model (black) for a single pixel.

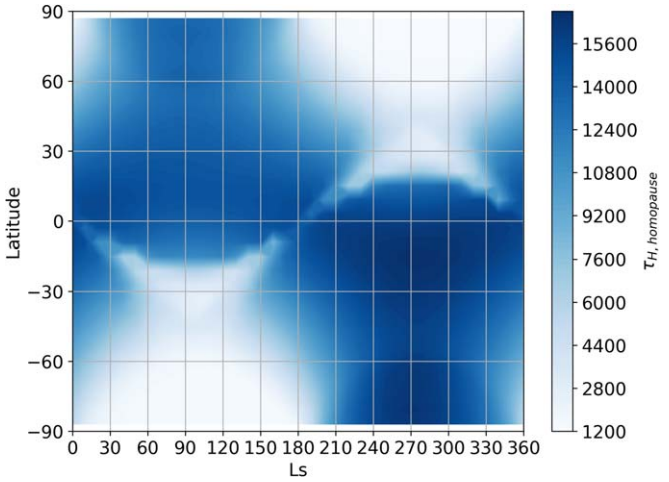

Figure 9. Optical depth of H above the methane homopause ($\tau_{CH4} = 1$) from the 2D photochemical model, similar to that from Moses & Greathouse (2005). The x-axis is solar longitude with the northern solstice occurring at $L_S = 90°$ and southern solstice at $L_S = 270°$.

driven by resonance scattering of solar flux by thermal atomic hydrogen.

2.4. Photochemical Models of Saturn's Upper Atmosphere

The upper atmospheric hydrogen is a probe of photochemistry deeper in the atmosphere, as it is primarily produced through photolysis of methane (Moses et al. 2000a), with only a small contribution from thermospheric chemistry. We compare the inferred H optical depths (outlined in Section 2.3) to two photochemical models: (a) 1D models tuned to the results of stellar occultations observed by Cassini/UVIS in 2016–2017 (Brown et al. 2020, 2024) and (b) a 2D model identical to Moses & Greathouse (2005), except we adopt solar-cycle average incident ultraviolet flux (including at Lyα), rather than tracking the ∼11 yr solar-cycle variation from the recent era.

1D models. Throughout 2016 and 2017, stellar occultations provided a pole-to-pole map of the thermosphere (Brown et al. 2020) and were used to retrieve temperature profiles as well as the densities of many atmospheric constituents (e.g., H_2, CH_4, Brown et al. 2024). However, as we noted before, it is not possible to retrieve the H density profile from stellar occultations, due to absorption of starlight by the interstellar medium. The H density profile is calculated with the 1D photochemical model, constrained by the profiles of other molecules.

For this study, we are interested in the hydrogen and methane profiles, particularly the H column above the methane homopause. We consider optical depths of $\tau_{CH4} = 1$ and $\tau_{CH4} = 10$ at Lyα, using a cross section of 1.79×10^{-17} cm^2 (Chen & Wu 2004). For the purposes of the comparison between the inferred optical depths and the model, the H optical depth is integrated above the homopause altitude for each occultation location, in line with the pressure-averaged temperatures above the homopause (see Figure 7).

2D model. We use the seasonally and meridionally varying 2D model of Moses & Greathouse (2005), which incorporates the time varying insolation to represent seasonal changes with solar-cycle averaged ultraviolet fluxes. In this model, the temperature–pressure profile is constant across latitudes and with season. It is important to note that this model parameterizes vertical transport by using an eddy diffusion profile that is constant with latitude and does not include any meridional transport. We integrate the H optical depth above the methane homopause ($\tau_{CH4} = 1$) as a function of latitude and time (with the time mapped to the solar longitude; see Figure 9). At present, photochemical models that account for seasonal changes to the temperature structure and mixing rates in the middle and upper atmosphere do not exist. The differences between the inferred H column from the Lyα observations and the photochemical model predictions identified in this study represent the first step to guide the development of such models in the future.

3. Results

3.1. A Comparison of UVIS Observations with the IPH Model

In this section, we compare observations of the IPH Lyα background throughout 2006 with modeled IPH brightnesses (see Figures 10 and 11). The set of observations is listed in Table 3. The brightnesses of the IPH observations have been scaled to the solar flux on 2009 Jan 1, when the solar activity was at a minimum. This corrects for variation of the IPH that results from the Sun's rotation. The scaled brightnesses are also given in Table 3. The modeled IPH brightnesses (black) agree well with the observations from Cassini/UVIS (blue), with an $R^2 = 0.64$. The brightness increases from 250 R in the antisunward direction ($\cos\theta_{Max} = -1$) to 650 R near the sunward direction ($\cos\theta_{Max} = 0.8$).

A cluster of eight points at $\cos\theta_{Max} = 0.4$ with $B = 250 \pm 40$ R is 100 R smaller than predicted by the model. However, there are several observations at similar angles with $B = 450$ R, suggesting the IPH model is not overestimating the brightnesses at this angle. Overall, the IPH observations by Cassini are consistent with the predictions of the IPH model at a heliocentric distance of 9.1 au.

3.2. Emission Trends of Saturnian Lyα from Multivariate Regression Analysis

Figure 12 shows the predicted brightnesses versus the actual observed brightnesses of Lyα for the multivariate regression model outlined in Section 2.2 for the testing data set (20% of points). The coefficients of the fit to Equation (1) are given in

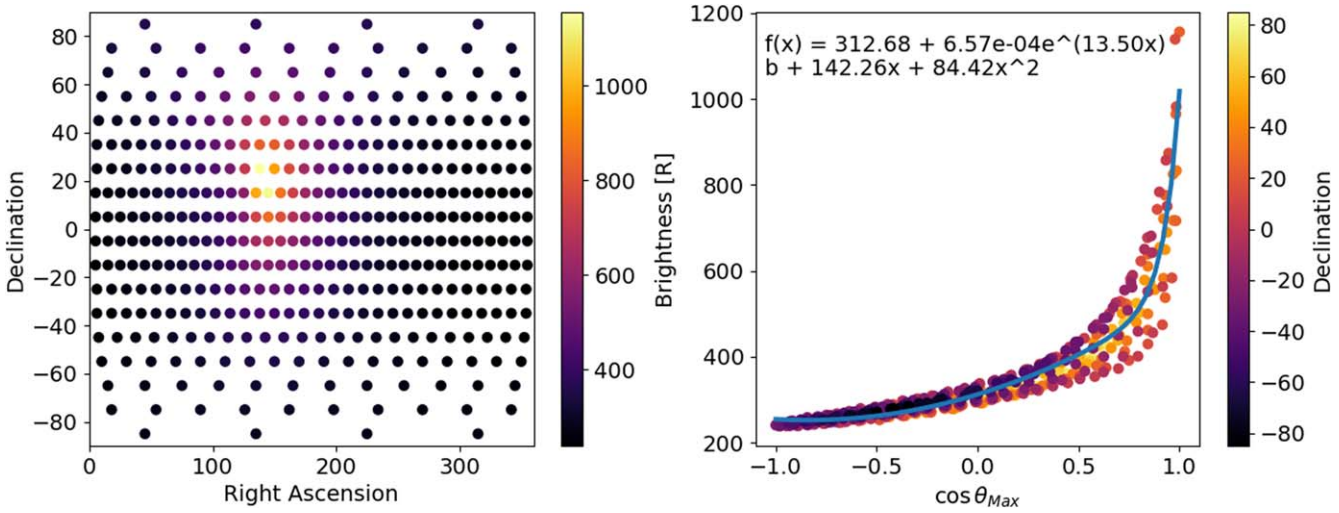

Figure 10. (Left) Full sky map of the modeled IPH brightness at Saturn in 2006 (see Section 2.3.2). (Right) Modeled IPH Lyα brightness against angle to direction of maximum brightness. The fit to the IPH brightness is shown in blue.

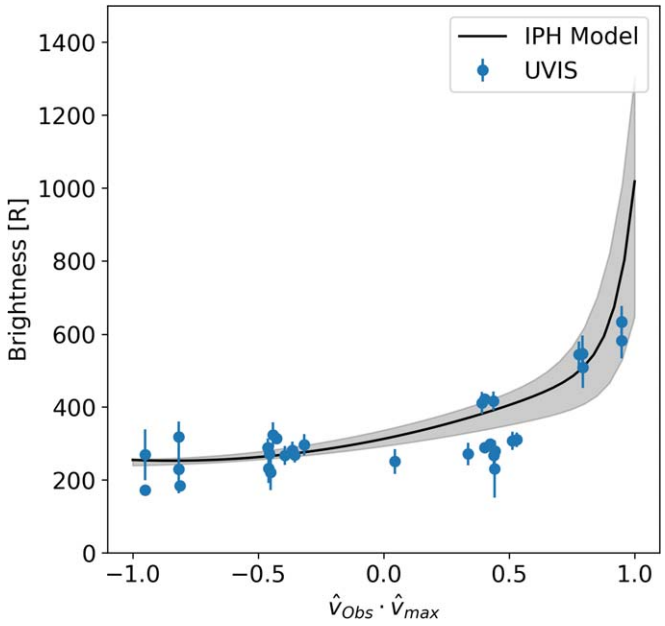

Figure 11. Comparison of IPH Lyα brightness from Cassini/UVIS observations throughout 2006 (blue) with the modeled brightness from the IPH background model (black, see Section 2.3.2 and Figure 10). The x-axis is the cosine of the angle between the observation direction and direction of maximum brightness The black line gives the best fit, with the shaded region depicting minimum and maximum modeled values.

Table 1. The fit has an $R^2 = 0.791$ demonstrating that the observed brightness can be well parameterized by the latitude, incidence, and emission angle once the observed brightness is scaled with the time-dependent solar flux. The three-variable regression does not capture the brightnesses at small values, but above 250 R, the model accurately predicts the observed brightnesses.

Figure 13 shows the dependence of the brightness on each of the independent variables around the constant values of $[\theta_{em}, \theta_{in}, \phi_{lat}] = [30, 30, 20]^\circ$ with the observed brightnesses shown for points within 10% of the constant values. The Lyα brightness is most strongly dependent on the incidence angle of light arriving from the Sun, with the brightness decreasing strongly from the subsolar point ($\theta_{in} = 0$) to the terminator plane at $\theta_{in} = 90$. Conversely, the brightness increases with emission angle, with the brightest regions near the limb of Saturn's disk. The dependence on the incidence angle closely fits a $\cos\theta_{in}$ dependence.

Figure 14(a) shows the radiation field predicted by the trained model at a latitude of 20°N, with the combined dependence of the brightness on the incidence and emission angles. It again demonstrates substantial darkening toward the terminator and brightening of the disk near the limb. The dependences of the observed brightness on latitude, emission, and incidence angles are consistent when using different multivariate regression models, such as support vector regression using radial basis fields.

In Figure 12(b), there is nonlinearity to the residuals, with a slight parabolic shape between 200 and 1000 R. Beyond 1000 R, the MVR model overestimates the observed brightnesses, but the statistics at these values are much lower (<150) compared to the intermediate brightnesses (200–1000 R). The structure in the residuals is not replicated when considering the behavior with respect to the independent variables (Figure 13). Each variable shows no discernable behavior in the residuals, suggesting higher order terms for each variable are not required.

Figure 14(b) similarly shows the modeled brightness of Lyα from the radiative transfer model (Section 2.3) at a temperature of 350 K and an atomic hydrogen optical depth of $\tau_H = 10{,}000$. The trained MVR model shows very similar behavior to the brightness from the RT model, with a bright limb and dark terminator region, indicating that the observed brightnesses can be mostly explained by resonance scattering of Lyα by upper atmospheric atomic hydrogen. The MVR and RT model differ in two main areas: the bright limb of the RT model and the increase in brightness at low emission angles observed in the MVR model. The very bright limb observed in the RT model is a result of the plane-parallel assumption, which breaks down near the terminator and near the limb of the disk. With a plane-parallel model, the gas column the photons travel through is greatly overestimated at the limb, inflating the modeled brightness. The increase in brightness at low emission angles for the MVR may be a result of the limited data available at small emission angles (see Figure 15), which do not strongly

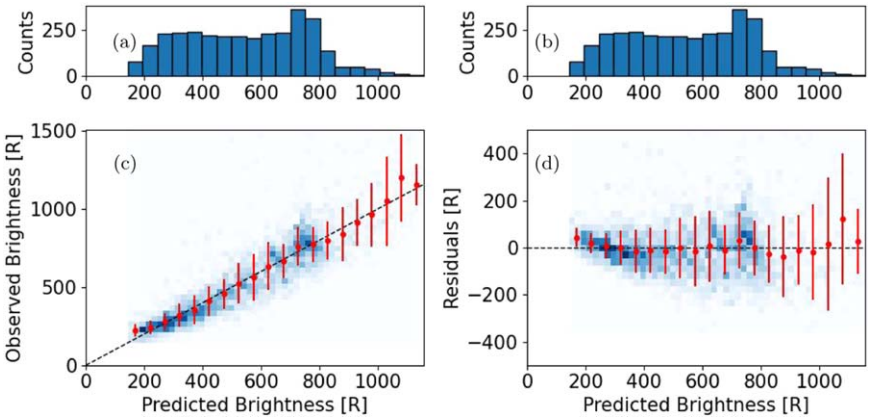

Figure 12. (a), (b) Testing data counts vs. predicted brightness from the MVR. (c) Observed brightnesses and (d) residuals vs. predicted brightnesses for the testing data set (blue) with the averages and standard deviations shown in red.

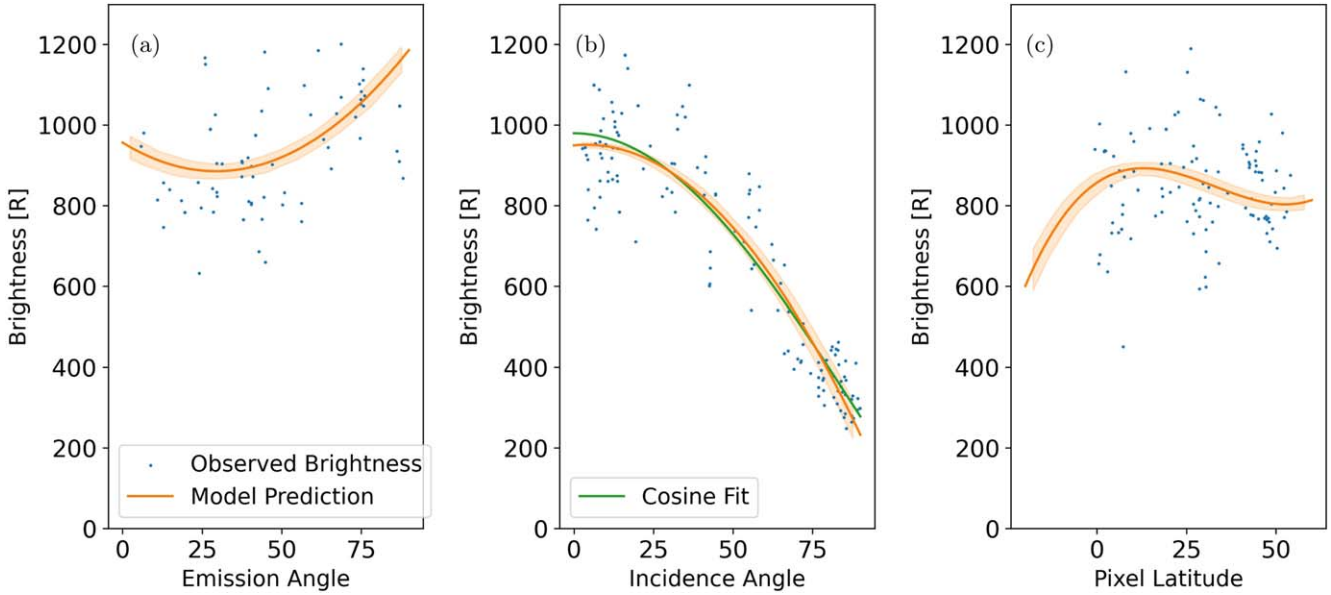

Figure 13. Comparison of the observed brightnesses from 2014–2017 in the testing data set (blue) to the multivariate regression predictions (orange) as a function of (a) emission angle, (b) solar incidence angle, and (c) latitude. The observed data are within the intervals $\theta_{em} = [27, 33]$, $\theta_{in} = [27, 33]$, and $\phi_{Lat} = [18, 22]$ for the other two independent variables. In panel (b), the best fit of a cosine to the observed brightnesses is given (green).

Table 1
Coefficients for the Fit Used in the Multivariate Regression (See Equation (1)), for the 2014–2017 Observations

Variable	Coefficient	Mean Value	Confidence Interval
Constant	p_0	6.51×10^2	$(6.49 \times 10^2, 6.53 \times 10^2)$
θ_{em}	p_1	3.73×10^0	$(3.68 \times 10^0, 3.77 \times 10^0)$
θ_{in}	p_2	-1.01×10^1	$(-1.02 \times 10^1, -1.01 \times 10^1)$
ϕ_{lat}	p_3	-3.54×10^0	$(-3.64 \times 10^0, -3.44 \times 10^0)$
θ_{em}^2	p_4	7.95×10^{-2}	$(7.74 \times 10^{-2}, 8.17 \times 10^{-2})$
$\theta_{em} \cdot \theta_{in}$	p_5	3.05×10^{-2}	$(2.85 \times 10^{-2}, 3.25 \times 10^{-2})$
θ_{in}^2	p_6	-9.36×10^{-2}	$(-9.54 \times 10^{-2}, -9.17 \times 10^{-2})$
ϕ_{lat}^2	p_7	2.52×10^{-2}	$(2.25 \times 10^{-2}, 2.80 \times 10^{-2})$
ϕ_{lat}^3	p_8	2.55×10^{-3}	$(2.43 \times 10^{-3}, 2.66 \times 10^{-3})$

constrain the observations at low emission and incidence angles.

The latitudinal variation seen in Figure 13(c) has been disentangled from the variation with the geometry of the observations without reliance on a radiative transfer model. The northern hemisphere bulge at low latitudes is a result of a meridional structure in the upper atmosphere. Using the same analysis for the 2004–2006 period, the latitudinal profile shows the reverse trend, with the bulge appearing near 20°S (see Figure 16). The brightness also decreases into the winter hemisphere and toward the summer pole. This shows a clear reversal with season in the latitudinal behavior, and shows that the bulge is not a permanent feature of the northern hemisphere. Instead, it is a seasonally changing feature that appears in the summer or spring hemisphere.

The source of the increased brightness at 20° in the summer hemisphere could be driven by either enhanced H column in the region or additional sources of emission within the bulge region. We split the data set into latitude bins of 10° and applied the same multivariate regression (see Figures 29 and 35). At all latitudes, the same dependence of the brightness on solar incidence and emission angles was observed, with $R^2 > 0.7$ and $R^2 > 0.6$ throughout northern and southern summers respectively. Some latitude bins were limited by the phase space coverage of the data (Figures 15, 30, and 36), with

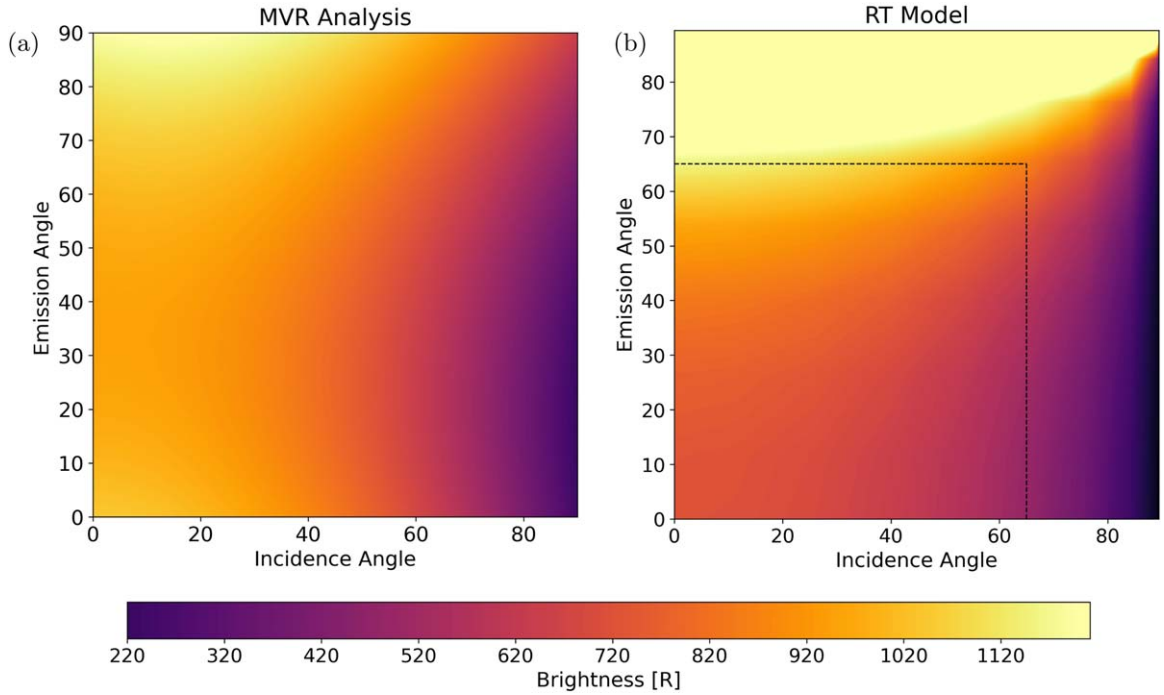

Figure 14. (a) Predicted brightness as a function of solar incidence and emission angles from the MVR analysis at a latitude of 20°N for the 2014–2017 data set. (b) Modeled brightness as a function of solar incidence and emission angles from the radiative transfer model (see Section 2.3) for an optical depth of $\tau_{\rm H} = 10{,}000$ and $T_{\rm Sat} = 350$ K. The dashed lines illustrate the region in which we compare observations to the radiative transfer model in Section 3.3.

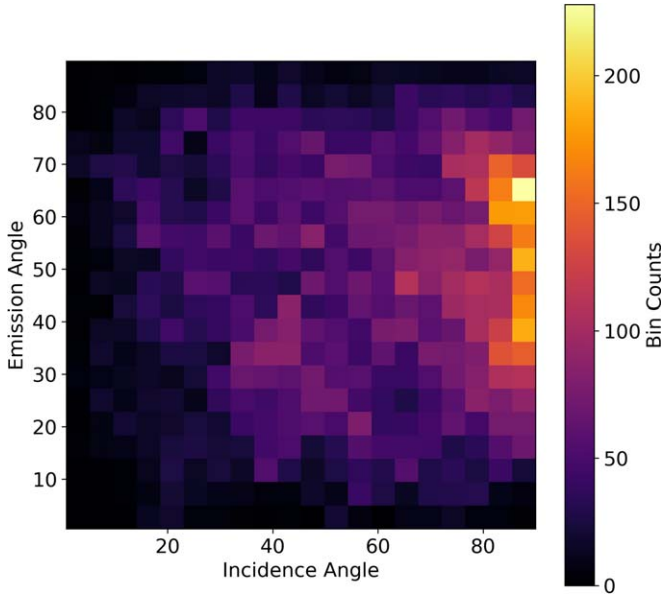

Figure 15. Histogram of observation geometries (solar incidence angles and emission angles) in the training data set for the multivariate regression from 2014–2017 (see Figures 13 and 14). Regions with fewer observations are less well constrained in the MVR model.

small emission angles not probed in the winter hemisphere or close to the poles. The consistency of the relation between the incidence and emission angles with latitude implies that there is not a substantial additional internal emission source in the northern hemisphere bulge. Therefore, the variation in Lyα brightness can likely be attributed to variation of the H column above the methane homopause. The alternative would be to attribute the variation to a seasonal change in the hot atomic H population, although no source of hot atoms that would have the required behavior has been identified to date.

3.3. Seasonal Variation of Saturn's Atmosphere

3.3.1. A Case Study of Northern Hemisphere Summer

We consider first an observation of Saturn on 2016 March 25, when the subsolar latitude was 26.°0, with incidence and emission angles from 0° to 65°. We exclude latitudes poleward of 60°, and in the ring shadow region that extends from 14°S to the south pole. This includes 1617 pixels across the dayside region highlighted in Figure 17, accumulated over 4.5 hr. The observed brightness is constant between the latitudes of 0° and 20°N at 596 ± 15 R, before decreasing to 518 ± 12 R 26°N–60°N. The observed brightness also drops sharply to 421 R at 9.4°S toward the ring-shadowed region (see Figure 18).

The modeled brightness for a constant H Lyα line center optical depth (hereafter, the H optical depth) of 10,000 also shown in Figure 18 agrees well with the brightness between 0° and 25°, but outside this range, the modeled brightness increases in contrast to the observation. The increased brightness is a result of larger emission angles for the southern and higher latitudes. The scattered Lyα from the IPH background has a fairly constant contribution of 78.5 ± 4.4 R across latitudes, which is 12% of the brightness of the scattered solar flux.

Figure 18(b) shows the H optical depths retrieved from comparison of the observations with the RT model. The close agreement between the modeled and observed brightness between 0° and 25° is reflected by the constant optical depth of $10{,}800 \pm 300$ R over this range. Northward of 25°N, the optical depth decreases continuously toward $\tau = 5000$ at 60°N, as the observed brightness declines relative to the expected values from the RT model based on constant H optical depth.

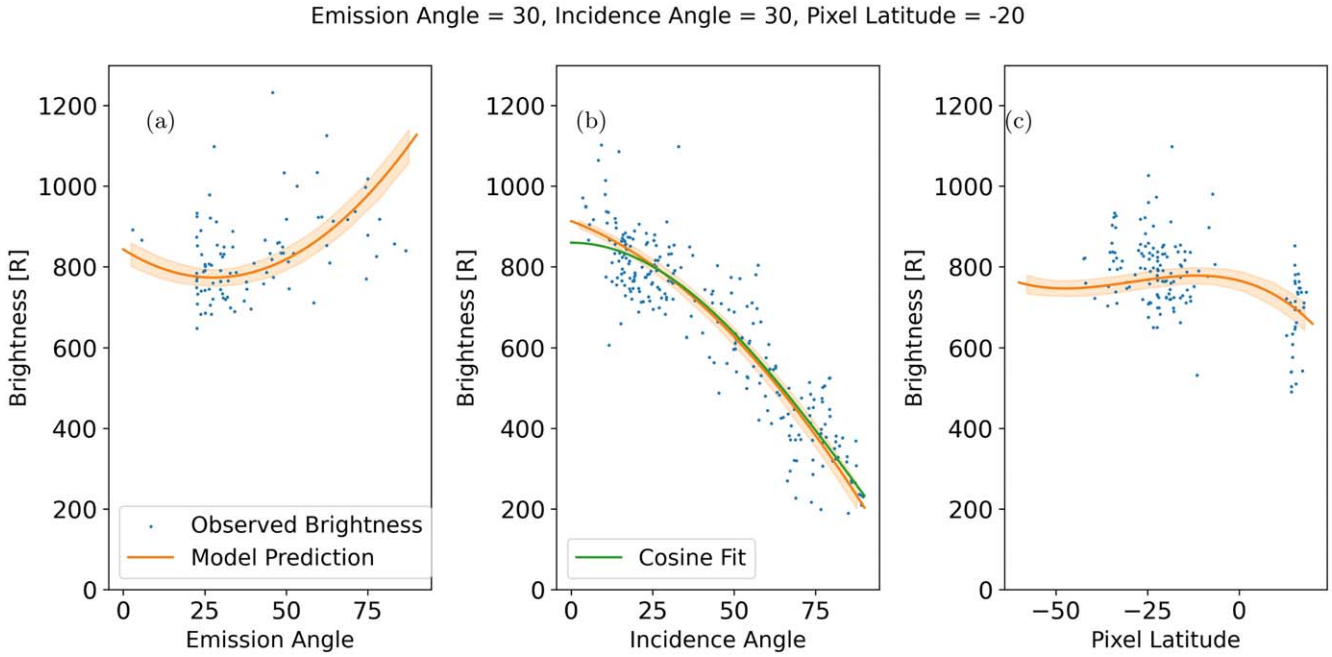

Figure 16. Comparison of the observed brightnesses in the 2004–2006 testing data set (blue) to the multivariate regression predictions (orange) as a function of (a) emission angle, (b) solar incidence angle, and (c) latitude. The observed data are within the intervals $\theta_{em} = [27, 33]$, $\theta_{in} = [27, 33]$, and $\phi_{Lat} = [-22, -18]$ for the other two independent variables. In panel (b), the best fit of a cosine to the observed brightnesses is given (green).

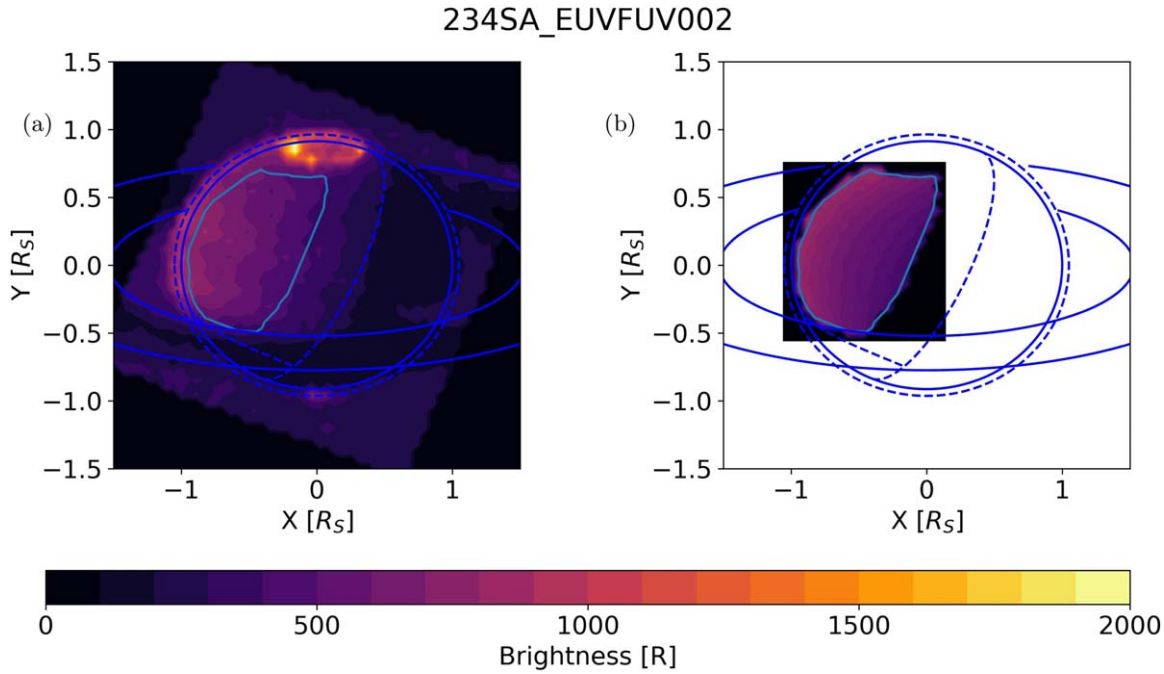

Figure 17. (a) Lyα brightness in observation 234SA_EUVFUV002, with the ring geometry, limb, and terminator of Saturn highlighted in blue. The considered region for comparison to the radiative transfer model is bounded by the light blue line. (b) Modeled Lyα brightness using $\tau_H = 10{,}000$ and the temperature dependence in Figure 7 in the RT model (see Section 2.3).

This decrease in the H optical depth is not predicted by the 1D photochemical model, which predicts that the H optical depth is approximately constant at 10,000 up to 60°N. However, the 2D photochemical model (orange) does show a slight decrease in the H optical depth from the peak at 10°N, but only by 10%, compared to the 50% reduction retrieved from the UVIS data. Southward of the equator, the H optical depth sharply decreases between 5.6°N and 9.4°S latitude toward the ring shadow, in close agreement with the photochemical model.

3.3.2. A Case Study of Southern Hemisphere Summer

Figures 19 and 20 show results for an observation from 2004 November 8, during the southern hemisphere (SH) summer, with a

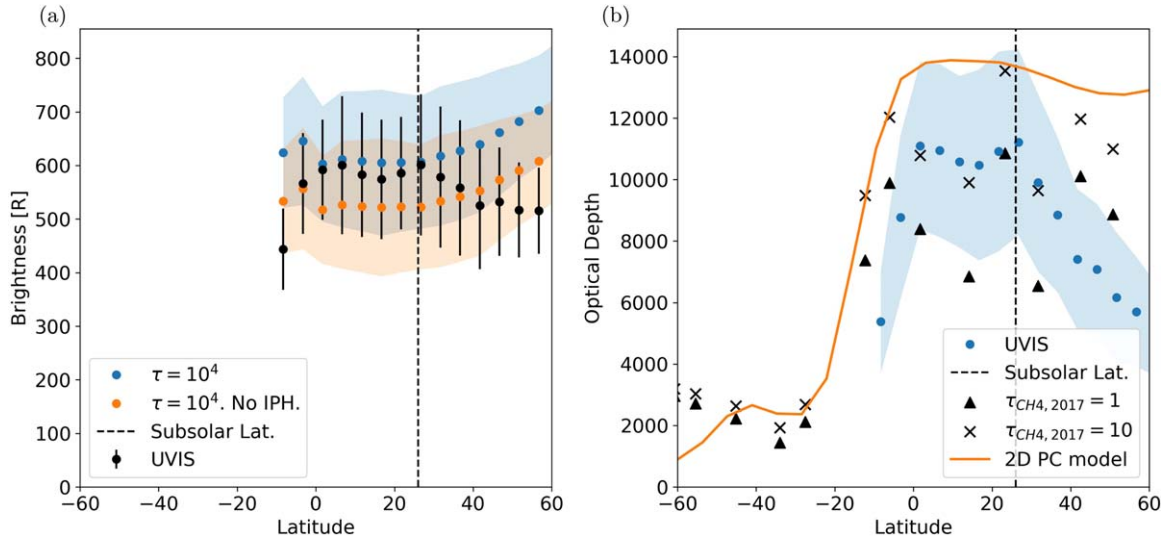

Figure 18. (a) Observed Lyα brightness (black) for observation 234SA_EUVFUV002 against latitude. The modeled brightness for the observation geometry using $\tau = 10{,}000$ and the temperature variation in Figure 7 is shown with (blue) and without (orange) the contribution of scattered IPH Lyα. (b) Optical depth (blue) vs. latitude retrieved from comparison of Cassini/UVIS observations. The optical depths of the methane homopause (using $\tau_{CH4} = 1$, triangles; and $\tau_{CH4} = 10$, crosses) predicted by 1D photochemical models tuned to 2017 stellar occultations are shown. (Orange) H optical depth from the 2D photochemical model on 2016 March 26 at subsolar latitude of 26.°0 and $L_S = 81.°2$ (see Figure 9).

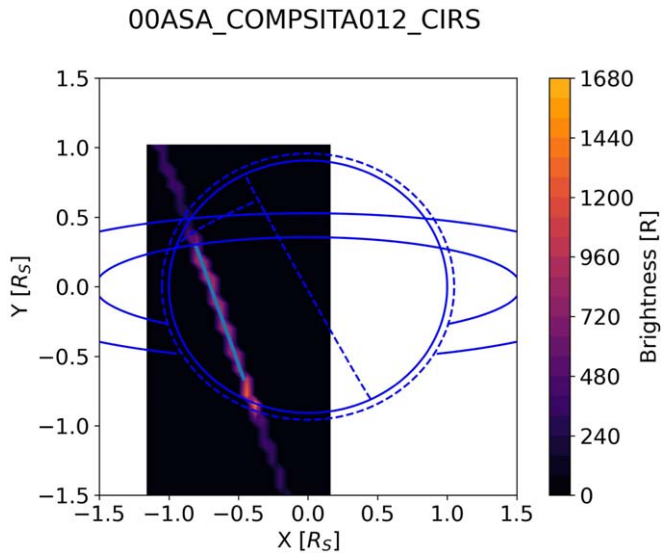

Figure 19. Observed Lyα brightness for the 00ASA_COMPSITA012_CIRS observation on 2004 November 8 with a subsolar latitude of $-23.°5$. The region modeled by the radiative transfer code is highlighted by the light blue line, with Saturn, the rings, and ring shadow regions superimposed in dark blue.

subsolar latitude of 23.5°S. The spatial coverage of Saturn's disk was much narrower for this case (see Figure 19), so the variation in the modeled brightnesses is much smaller at each latitude. The observed brightness decreases sharply from 1030 ± 38 R at 60°S to 780 ± 31 R at 40°S as a result of the decreasing emission angle. The lower brightness is closely matched by the modeled brightness based on constant H optical depth, and can be attributed wholly to changes in the viewing geometry.

The observations and constant H optical depth model, however, diverge between 40°S and the equator, with the modeled brightness continuing to decrease to 690 ± 7 R while the observed brightness increases to 888 ± 36 R in this region. The retrieved H optical depths (blue, Figure 20(b)) therefore increase substantially over this latitude range, peaking at $\tau_H = 17{,}500 \pm 2500$ at 13°S. Equatorward of the peak, the H optical depths decrease sharply toward the ring shadow region, closely mirroring the behavior observed in the northern hemisphere summer hemisphere (see Figure 18), and predicted by the 2D seasonal photochemical model (orange). The magnitude of the H optical depths in the summer hemisphere are also broadly consistent with the model, which predicts peak H optical depths of $\tau_H = 16{,}600$ at 3°S.

3.3.3. Implications for Upper Atmospheric Hydrogen

Having examined two observations from the NH and SH summers, we now apply the same analysis to all the dayside disk observations from Cassini/UVIS from 2004 through to 2016. We exclude 2017 as there is little coverage of Lyα emissions from the dayside Saturn disk. We have calculated H optical depths for each pixel (as outlined in Section 2.3) and taken annual averages and standard deviations. We have separated the SH summer (2004–2006, Figure 21), equinox period (2007–2010, Figure 22), and NH summer periods (2011–2017, Figure 23).

Much like in the case study (Figure 20), the annual averages exhibit a substantial latitudinal variation during the southern summer (Figure 21), with H optical depths increasing from 60°S toward the hydrogen bulge in the SH between 10°S and 25°S. Northward of the bulge, the H optical depth declines sharply with latitude. There are few available observations north of 20°N throughout 2004–2006, as these latitudes are typically obscured by either the rings or the ring shadow region. The sharp decrease in H optical depth around the equator is also observed in the photochemical model. The decrease in the H optical depth at the equator is shifted southward relative to the photochemical model, and the gradient shifts southward from 2004 to 2006. This may result from the movement of the southern boundary of the ring shadow, which begins at 6.°6–17.°3N in 2004 and reaches 4.°4–12.°3N in 2006. The peak H optical depth, seen in the southern hemisphere bulge, decreases from 2004 to 2006. There is substantially more variation than expected based on the photochemical model (Moses & Greathouse 2005), and this is discussed in Section 4.3.

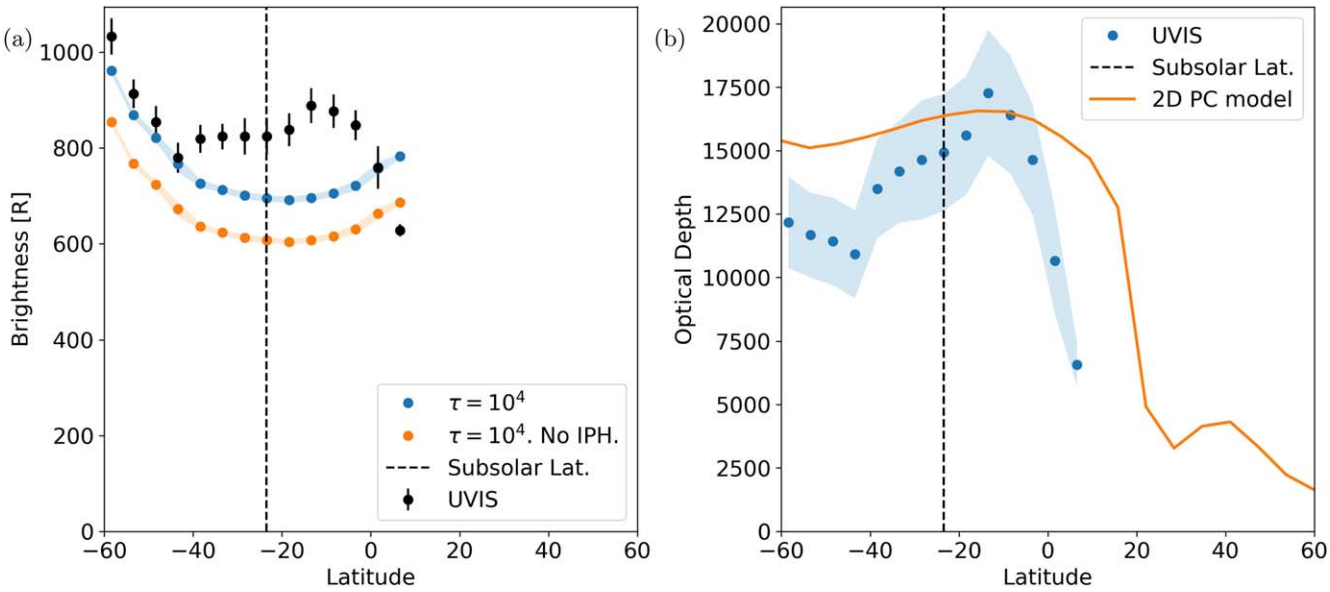

Figure 20. (a) Observed Lyα brightness (black) for observation 00ASA_COMPSITA012_CIRS against latitude. The modeled brightness for the observation geometry using $\tau = 10{,}000$ and the temperature variation in Figure 7 is shown with (blue) and without (orange) the contribution of scattered IPH Lyα. (b) Optical depth (blue) vs. latitude retrieved from comparison of Cassini/UVIS observations with the radiative transfer model. (Orange) H optical depth from the 2D photochemical model on 2004 November 8 at subsolar latitude of $-23.^{\circ}5$ and $L_S = 302^{\circ}$.

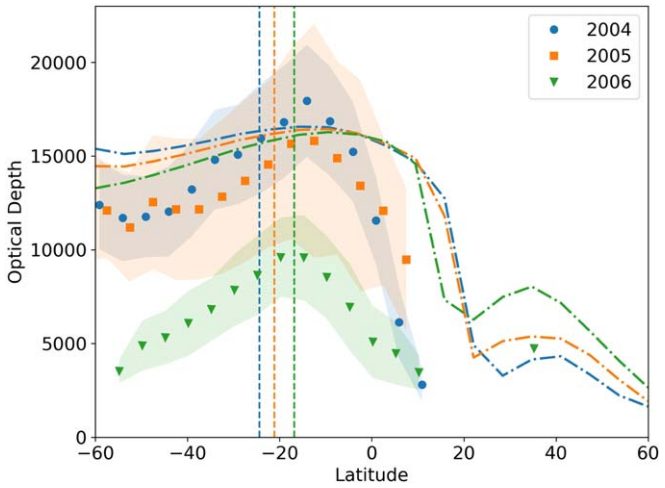

Figure 21. Yearly averages of the optical depths during the southern hemisphere summer (2004–2006; colored circles), with shaded regions showing the uncertainty (see Section 2.3). The subsolar latitude for each year is given by the dashed vertical lines. The dashed–dotted lines show τ_H predictions from the 2D photochemical model in each year.

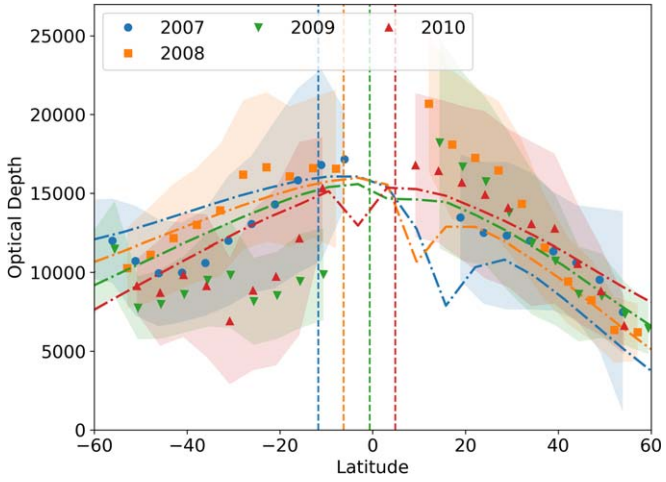

Figure 22. Yearly averages of the optical depths around equinox (2007–2010; colored points), with shaded regions showing the uncertainty (see Section 2.3). The subsolar latitude for each year is given by the dashed vertical lines. The dashed–dotted lines show τ_H predictions from the 2D photochemical model in each year.

During the equinox period (Figure 22), the H optical depths increase continuously from the polar regions at $\pm 60^{\circ}$ toward the equator. They agree well with the modeled depths from the 2D photochemical model (dashed–dotted lines) in both magnitude and meridional structure. The equatorial latitudes have been excluded as they are obscured by the ring shadow and ring atmosphere during these years. The observed brightness decreases around the equator, but we cannot determine whether the H column is smaller due to the uncertainty in the illumination conditions. The H optical depths throughout this period show less variation than seen in the summer hemisphere (Figures 21 and 23), particularly in the northern hemisphere where the maximum H optical depth is $\tau_H = 17{,}200 \pm 2300$.

In the southern hemisphere during the equinox period, the peak H optical depths are similar, except in 2009 and 2010, which both exhibit significantly reduced H optical depths at midlatitudes. The lower brightnesses compared to 2007 and 2008 are unexpected, much like the substantial variation during the southern hemisphere summer. The retrieved H optical depths are also 40% smaller than the photochemical model predictions at 20°S. We note that the highest optical depths are not consistently located in the more illuminated hemisphere. While this is the case in 2007 and 2010, the optical depths in 2008 are largest in the northern hemisphere despite a subsolar latitude of 6°S.

During the northern summer (Figure 23), the hydrogen bulge has shifted from the southern hemisphere (Figure 21) to the northern hemisphere, along with the subsolar latitude. The H optical depth decreases continuously toward 60°N, as seen in the case study (Figure 20). From 2011–2013, the southern hemisphere is not completely shadowed by Saturn's rings. The

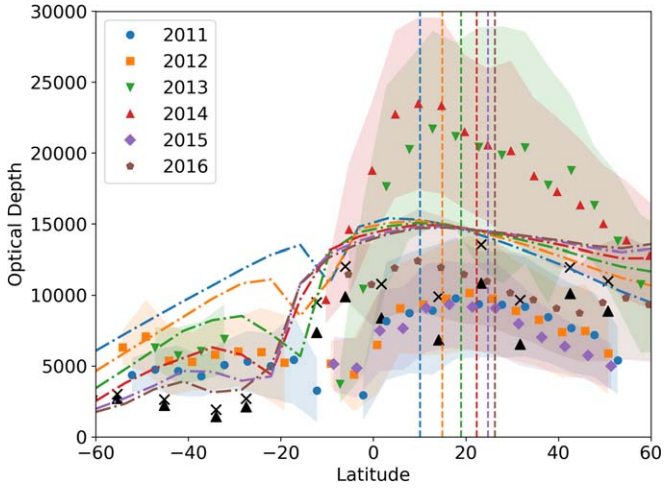

Figure 23. Yearly averages of the H optical depths during the northern hemisphere summer (2011–2016, colored points), with shaded regions showing the uncertainty (see Section 2.3). The subsolar latitude for each year is given by the dashed vertical lines, with the corresponding color. (Black points) H optical depths above the methane homopause (at $\tau_{CH4} = 1$, triangles; and $\tau_{CH4} = 1$, crosses) from 1D photochemical models based on 2017 UVIS occultations (see Section 2.4). The dashed–dotted lines show τ_H predictions from the 2D photochemical model in each year.

retrieved H optical depths are roughly constant at $\tau_H = 5000$ in the winter hemisphere and much smaller than the northern hemisphere peaks. This is also in good agreement with the 1D models based on 2017 stellar occultations (see Section 2.4), which predicted H optical depths of $\tau_H = 3000$ in the shadowed winter hemisphere. As seen during the earlier periods, there is substantial variability in the peak H optical depths over time. Large H optical depths of $\tau_H = 22{,}100 \pm 6990$ and $\tau_H = 24{,}000 \pm 6200$ are observed in 2013 and 2014, while in 2012 and 2015 the peak H optical depths are $\tau_H = 10{,}000 \pm 4100$. The H optical retrieved from the observations in 2013 and 2014 is twice as large as those predicted by the 1D photochemical models and 50% larger than the predictions of the 2D model.

4. Discussion

4.1. Source of Lyα Emissions

The multivariate regression analysis of the Lyα brightness observations strongly supports the dominance of resonance scattering as the source of nonauroral Lyα emissions, with scattered solar flux comprising the majority of the observed emissions. The strong dependence of the Lyα brightness on the solar incidence angle (see Figure 13(b)) demonstrates the importance of solar photons in generating the observed emissions. Scattered photons from the IPH background would have a much weaker dependence on solar incidence angle, as they enter the atmosphere from all directions. Potential internal sources of Lyα photons would also not exhibit the variation with solar incidence angle, such as the electroglow proposed by Shemansky et al. (2009) and others. While solar flux dominates, the contribution of scattered IPH Lyα photons is important for estimating the H optical depth.

The radiation field retrieved through the multivariate regression analysis remains consistent across latitudes and mission periods. At all latitudes, the observed brightness can be fit with a quadratic function of incidence and emission angles, with the brightness decreasing strongly toward larger incidence angles. For internal sources of emissions, we would not expect a strong dependence on solar incidence angle. The peak in the brightness and optical depth at latitudes of 10°–20° in the summer hemisphere is therefore unlikely to be driven by an internal emission source. Our results, however, do not discount the possibility of hydrogen or water entering the upper atmosphere from the rings in the equatorial region, such as that detected by INMS (Waite et al. 2018; Yelle et al. 2018; Serigano et al. 2020, 2022), and leading to local increases in the H density, although Cassini/UVIS occultations and photochemical modeling during the Grand Finale do not suggest that a substantial fraction of the influx materials vaporize in the thermosphere (Moses et al. 2023). A smaller suprathermal (25,000 K) hydrogen population (0.1% of the ambient H) could drive substantial emissions. The existence of such a population is currently hypothetical but can be better constrained with detailed modeling of emission profiles from Saturn's limb. Assuming no hot hydrogen population, the τ_H variation is similar to that predicted by the 2D photochemical model, which predicts a sharp decrease in the H column in the winter hemisphere (see Figure 9). This strongly suggests that the low-latitude brightness peak is seasonal in nature and origin.

4.2. The IPH Model and Cassini/UVIS Calibration

The brightnesses predicted by our IPH model (Section 2.3.2) agree well in both viewing direction and magnitude with observations of the IPH Lyα emissions by Cassini/UVIS (see Figure 11).

A proposed recalibration of Cassini/UVIS at Lyα by a factor of 1.7 (Ben-Jaffel et al. 2023; Pryor et al. 2024) would result in much larger observed brightnesses for the IPH (1255 R at $\cos\theta_{Max} = 0.94$) compared to those predicted by the IPH model (762 R). This would require a significant increase in the hydrogen density at the termination shock, or galactic emissions beyond the scale of current estimates (Gladstone et al. 2021). The angular dependence of the disparity could not be rectified by additional galactic Lyα flux. We note that Ben-Jaffel et al. (2023) obtained the calibration factor by comparing Cassini/UVIS observations with Saturn disk brightnesses observed by HST/STIS in 2017 from Earth orbit. There were, however, no simultaneous dayside observations of Saturn's disk obtained by Cassini/UVIS in 2017, and the comparison also depends on viewing geometry as indicated here. The required corrections for IPH absorption and geocorona also make it difficult to extract the line shape from HST/STIS observations.

Our IPH model, which is constrained by observations of New Horizons Alice, Bepi/Colombo PHEBUS, and SWAN (Izmodenov et al. 2013; Quémerais et al. 2013a), predicts the brightness of the IPH Lyα to reach 250 R in the antisunward direction during the 2006 observations and rise to 900 R in the sunward direction. The good agreement between the model and UVIS observations suggests that the calibrations of Cassini/UVIS and the three other instruments are consistent.

4.3. Seasonal Variability in Thermospheric Atomic Hydrogen

Assuming that a population of hot atoms is not significant, the H optical depths retrieved from the UVIS observations with the RT model (see Section 3.3) agree well with the optical depths predicted by the photochemical model. The peak in brightness, identified in the northern hemisphere by Ben-Jaffel et al. (2023), translates to an increase in the atomic hydrogen

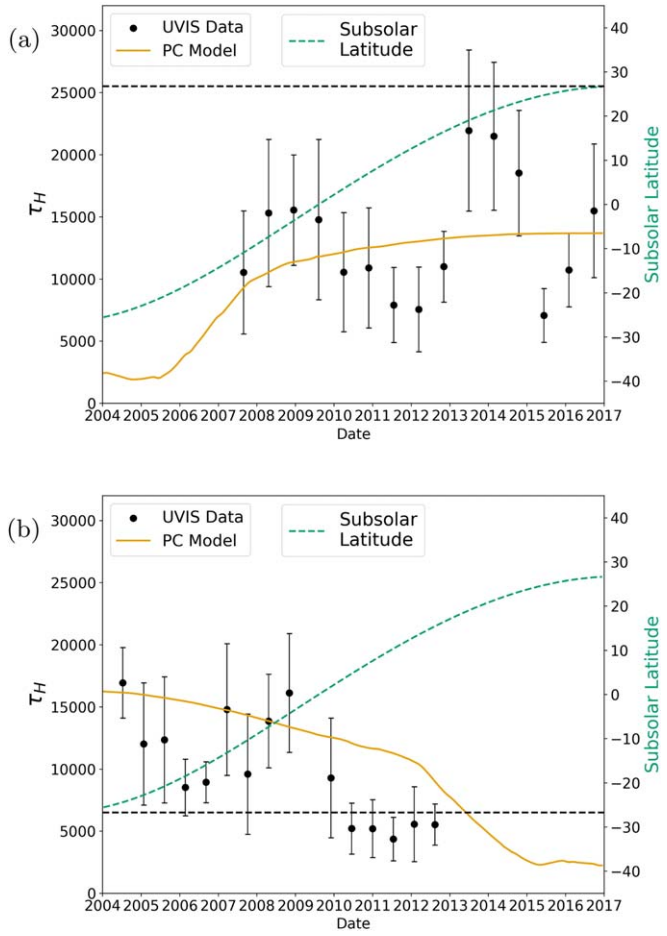

Figure 24. (a) Optical depth at 26.7°N ±5° (northern solstice latitude, black dashed line), throughout the Cassini mission from the (black) UVIS observations and RT model comparison (see Section 2.3) and (orange) the 2D photochemical model (see Section 2.4). The subsolar latitude is shown in green. (b) The same as above but for −26.7 (southern solstice latitude).

optical depth above the methane homopause. However, the bulge at 20°N is not a permanent feature of the northern hemisphere, but shifts with season and is observed in the southern hemisphere during the southern summer (see Figure 21). A similar peak in the H optical depth is also predicted by the 2D photochemical model, which clearly shows a reversal in season (see Figure 9).

The poleward decrease in H optical depth from 20° to 60°N in the northern summer is also predicted by the 2D photochemical model (Figure 9), although not to the same extent as estimated by the UVIS/RT model comparison. The poleward decrease disagrees with the 1D photochemical models, which were tuned to stellar occultations in 2017 (black points, Figure 23; Brown et al. 2024). These models do not show a significant decrease in the H optical depth toward higher latitudes, and also do not exhibit the same bulge around 20°N. The magnitude of the H optical depths is consistent with the results of the photochemical models (both 1D and 2D) with typical optical depths between $\tau_H = 5000$–15,000 (see Figures 9, 20, and 23). The proposed revision of the Cassini/UVIS sensitivity by Ben-Jaffel et al. (2023), increasing observed Lyα brightnesses by a factor of 1.7, would result in more significant enhancements in the retrieved optical depths. While the latitudinal and seasonal trends would be unaffected, the nonlinear relationship between optical depth and brightness (see Figure 3) would see an increase of 2.5 to 3× in the H optical depth compared to the current estimates. As a result, the retrieved hydrogen column densities would be inconsistent with either the 1D or 2D photochemical models, albeit at the same time roughly following the seasonal behavior predicted by the models.

The proposed calibration factor means that an additional emission source or an alternative source of H would be required. The strong dependence of brightness on solar incidence angle, identified in the multivariate regression (see Section 3.2), excludes an emission source of the required magnitude other than resonance scattering of solar flux. While an additional source of hydrogen is not excluded by the current analysis, the magnitude of atomic H required would be beyond the estimates of what is possible from equatorial ring inflow (up to 1.75×, Ben-Jaffel et al. 2023), and would be required planetwide. Photochemical modeling suggests that ring rain entering the atmosphere as solid particles is unlikely to vaporize and contribute to the background gaseous atmosphere, and therefore should not significantly enhance the H column. A smaller population of hot H in the thermosphere is not excluded by our analysis but remains unidentified.

The year-to-year variability of the optical depths retrieved, however, is highly unexpected, with variation by a factor of 2 observed from one year to the next (see Figure 24). The 2D photochemical model (orange), which incorporates the variation of the subsolar latitude but neglects EUV solar-cycle variation, predicts minimal short-term variation of the H column above the homopause. Between solar minimum and maximum, a variation by about a factor of 2 is expected in the H column (Ben-Jaffel et al. 2023), but on the shorter timescales of the observed behavior, the variability of the H optical depth is far greater than expected.

To illustrate the variability, Figure 24(a) shows the optical depth at 26.7 ± 5°N and Figure 24(b) for 26.7 ± 5°S, the subsolar latitudes of the northern and southern hemisphere solstices. At 26.7 ± 5°S, the 2D photochemical model predicts a continuous and monotonic reduction in the H optical depth above the methane homopause from 2004 to the end of the mission in 2017, while the reverse is true for the northern hemisphere.

The retrieved H optical depths from Cassini/UVIS show the same overall trend with time for $\phi_{lat} = 26.7$°S, initially large at values of $\tau_H = 18{,}000$ and subsequently decreasing into the NH summer, when the ring shadows much of the southern hemisphere. However, the optical depth appears to oscillate around a mean value similar to the photochemical model. The trend is repeated in the northern hemisphere, with a sinusoidal time dependence around the photochemical model average. This indicates that there may be additional time-dependent behavior that is modifying the upper atmospheric hydrogen content with a timescale of several years. The source of this time-variability is not incorporated into the photochemical model and requires further investigation.

The solar cycle is a natural candidate for this temporal dependence, which was at a minimum in 2009 and peaked in 2013 and 2014 (see Figure 5). The variation of the UV flux could modulate chemistry (e.g., methane photolysis) and temperature profiles in the thermosphere leading, which in turn would impact the upper atmospheric hydrogen. While some years could be explained by this process (e.g., large optical depths in 2014, Figure 23), the variation of the

thermospheric hydrogen often bucks trends with the solar cycle (e.g., 2015 versus 2016). As such, there is likely an alternative or additional driver of changes in the thermosphere.

One possible source of the variation in the inferred H optical depths could be changes in the thermospheric temperature. The 2D seasonal photochemical model does not include temperature changes with either season or latitude. Occultations and circulation models have shown that thermospheric temperatures vary both seasonally and meridionally (Müller-Wodarg et al. 2019; Brown et al. 2020; Koskinen et al. 2021). Increases in thermospheric temperatures lead to increases in the scale height and the brightness from resonant scattering of solar flux. The factor of 2 variation in the inferred optical depth (see Figure 24) could be reconciled by a 40% temperature change (i.e., 350–500 K), for the same density of H above the methane homopause. For example, a temperature variation of the order of 150 K between 2006 and 2017, with a peak temperature around 2010–2012, has been observed in the middle thermosphere around the equator in the UV occultation data (Koskinen et al. 2021). In addition, the homopause depth likely changes over time, due to the effect of the changing seasons on dynamics in the middle atmosphere. For example, downwelling near the homopause would drive methane deeper in the atmosphere and increase optical depths. Disentangling the possible drivers of atomic hydrogen variability will require a seasonal model in which the temperature structure and homopause depth also change with time, combined with an analysis of the occultations, H_2 emission data, and limb scans from the duration of the Cassini orbital mission. We note that the analysis of solar occultations and limb scans can be used to retrieve vertical profiles of H and therefore further constrain additional degradation of the Cassini/UVIS instrument and calibration at Lyα.

5. Conclusion

We have examined the extensive data set of Lyα emissions from the Saturn disk throughout the Cassini mission, as well as observations of Lyα emitted from IPH background. We compared the IPH Lyα observations with the model of Quémerais et al. (2013a), which is calibrated with observations from SWAN, New Horizons Alice, and other platforms (Izmodenov et al. 2013; Quémerais et al. 2013a). The Cassini/UVIS observations and the IPH model agree well with each other, suggesting that the calibration of Cassini/UVIS at Lyα is consistent with the instruments underlying the IPH model.

We applied a multivariate regression analysis to the observed brightness throughout the mission, to disentangle variations as a result of observation geometry and those from meridional changes in the atmosphere. The emission brightness from Saturn's disk is dependent on four key variables: solar flux at the top of the atmosphere, latitude, and the emission and incidence angles applicable to the observations. The dependence of the observed Lyα brightness on the emission and incidence angles agrees closely with a model of resonant scattering of solar photons, exhibiting a strong decrease of the observed brightness with increasing solar incidence angle. We therefore exclude the possibility of a substantial internal source of Lyα emissions outside auroral regions.

We observe a bulge in the Lyα emissions in both the northern and southern hemispheres, during their respective summer seasons. Therefore, we conclude that the bulge previously reported by Ben-Jaffel et al. (2023) in the northern hemisphere during spring and summer is a seasonally modulated feature. Around the equinox, the Lyα brightness and effective H optical depths increase toward the equator (once the ring and ring shadow are excluded) in both hemispheres, giving the equatorial region an appearance of a bulge.

We compared observations of Lyα emissions taken during the Cassini orbital mission to a radiative transfer model, using the model to retrieve estimates of the H optical depth above the strongly absorbing methane homopause level. The magnitude and latitudinal variation of the H column agree well with the predictions of the photochemical model (2D in particular), albeit with much more substantial temporal variability in the observations. A comparison of the temporal changes in the southern and northern hemispheres again shows further evidence of seasonal change in the upper atmospheric hydrogen, with a peak in the effective H optical depths at a latitude of 20° in the summer hemisphere. The atomic H column decreases sharply into the winter hemisphere toward the ring shadow and more gradually toward higher latitudes (60°). While the seasonal photochemical model of Moses & Greathouse (2005) predicts roughly constant peak optical depths of $\tau_H = 15{,}000$ with season, our peak optical depth estimates varied by up to a factor of 2 year to year. At latitudes of $\pm 26.^{\circ}7$, the optical depth appears to show a sinusoidal variation in time around the mean depth of the photochemical model, especially in the northern hemisphere. The source of this variation requires further examination.

Observations of emissions from the limb and terminator of the planet have been avoided in this study due to the plane-parallel assumption used in the radiative transfer model. Further work is required to analyze the limb and near-limb observations, which would provide a constraint on the vertical profile of the atomic hydrogen in the thermosphere. This would provide much greater constraints on the possibility of a suprathermal hydrogen layer in the upper atmosphere than nadir scans that probe the scattering by the bulk of the H column. Additionally, the Lyman and Werner bands of H_2 and He 584 Å line emission should also be addressed to infer constraints on energy deposition as well as the H_2 and He densities in the upper atmosphere.

Acknowledgments

P.S., T.T.K., and J.M. acknowledge support by the NASA Cassini Data Analysis Program grant 80NSSC22K0306. Z.B. acknowledges support by the NASA/CDAP grant 80NSSC19K0902. P.L. acknowledges support from the project ATMOHAZE within the framework of the CNRS-UArizona collaboration initiative Searching for Habitable Worlds, in the solar system and beyond.

Appendix A
Radiative Transfer Model

The radiative transfer model is a plane-parallel model based on iterative doubling and adding of layers. Two layers of the atmosphere, A and B with A above B (see Figure 25), are combined with

$$U_A = S_B \exp\left[-\tau_A \frac{\psi(x_{\rm in}) + \bar{\omega}_a}{\mu_{\rm in}}\right] + S_B \cdot D_A \qquad \text{(A1)}$$

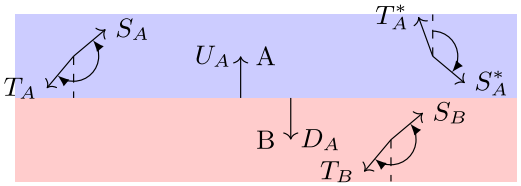

Figure 25. Diagram of layers A and B, with optical depths τ_A and τ_B. Upward ($U_{A,B}$) and downward fluxes for each layer are shown, in addition to the scattering ($S_{A,B}$) and transmission functions ($T_{A,B}$). Starred variables are oriented opposite to the typical direction and are important for multiple scattering.

$$D_A = T_A + S_A^* \cdot U_A \tag{A2}$$

$$S_{A+B} = S_A + \exp\left[-\tau_A \frac{\psi(x_{\rm em}) + \bar{\omega}_a}{\mu_{\rm em}}\right] U_A + T_A^* \cdot U_A \tag{A3}$$

$$T_{A+B} = \exp\left[-\tau_A \frac{\psi(x_{\rm in}) + \bar{\omega}_a}{\mu_{\rm in}}\right] T_B + D_A \exp\left[-\tau_B \frac{\psi(x_{\rm em}) + \bar{\omega}_a}{\mu_{\rm em}}\right] + T_B \cdot D_A, \tag{A4}$$

where

1. U, $D = U$, $D(x_{\rm em}, \theta_{\rm em}, \phi_{\rm em}; x_{\rm in}, \theta_{\rm in}, \phi_{\rm in})$ are the upward and downward fluxes at the layer boundaries;
2. $x_{\rm em}$, $x_{\rm in}$ are the emitted and incident frequency;
3. θ, θ_0 are the angles of emission and incidence, with $\mu = \cos\theta$;
4. τ is the optical depth of a layer;
5. S and $T = S$, $T(\tau; x_{\rm em}, \theta_{\rm em}, \phi_{\rm em}; x_{\rm in}, \theta_{\rm in}, \phi_{\rm in})$ are the scattering and transmission functions for each layer with the starred values indicating they are defined opposite to the typical direction (scattering is typically upwards, transmission downwards);
6. $\psi(x)$ is the Lyα lineshape, characterized by a Voigt profile at the upper atmospheric temperature;
7. $\bar{\omega}_a$ is the absorption albedo, which has been set to 0 throughout.

We note that Equations (A2) and (A3) differ slightly from Equations (8) and (9) in Yelle et al. (1989), as we more explicitly define the directions of the scattering function. The final term in Equation (10) of Yelle et al. (1989) is a typo and is corrected in Equation (A4).

The dot product is defined as

$$S_A \cdot U_A = \frac{1}{4\pi\mu} \int_0^{2\pi} d\phi' \int_0^1 d\mu' \int_{-\infty}^{\infty} dx' \times \{S_A(\tau_A; \boldsymbol{x}_{\rm em}; \boldsymbol{x}') U_A(\tau_A; \boldsymbol{x}'; \boldsymbol{x}_{\rm in})\}, \tag{A5}$$

where the vectors $\boldsymbol{x} = (x, \mu, \phi)$ for each set.

The brightness of scattered solar flux is given by

$$4\pi I_{\rm Sol}(\mu_{\rm em}, \mu_{\rm in})[R] = \Delta\nu_{D,\rm Sat} \times 10^{-6} \times \int_{-\infty}^{\infty} dx_{\rm in} \int_{-\infty}^{\infty} dx_{\rm em} S(\tau; \boldsymbol{x}_{\rm em}; \boldsymbol{x}_{\rm in}) F_{\rm Sol}(x_{\rm in}), \tag{A6}$$

where $F_{\rm Sol}$ is the solar Lyα flux incident on the atmosphere, with an incidence angle of $\theta_{\rm in}$. The Doppler width in Saturn's thermosphere is

$$\Delta\nu_{D,\rm Sat} = \frac{\nu_0 v_{\rm th}}{c} = \frac{\nu_0}{c}\sqrt{\frac{2k_{\rm B}T_{\rm Sat}}{m}}. \tag{A7}$$

Appendix B
Thin Layer Approximations

From Yelle (1988), we have the equation for the scattering function, S:

$$\begin{aligned}
&\left[\frac{\psi(x_{\rm em})}{\mu_{\rm em}} + \frac{\psi(x_{\rm in})}{\mu_{\rm in}}\right] S(\tau; \boldsymbol{x}_{\rm em}; \boldsymbol{x}_{\rm in}) + \frac{\partial S(\tau; \boldsymbol{x}_{\rm em}; \boldsymbol{x}_{\rm in})}{\partial\tau} \\
&= R(\tau; \boldsymbol{x}_{\rm em}; \boldsymbol{x}_{\rm in}) + \frac{1}{4\pi}\int_0^{2\pi} d\phi' \int_0^1 \frac{d\mu'}{\mu'} \int_{-\infty}^{\infty} dx' \\
&\quad \times \{R(\tau; \boldsymbol{x}_{\rm em}; x', \mu', \phi') S(\tau; x', \mu', \phi'; \boldsymbol{x}_{\rm in})\} \\
&\quad + \frac{1}{4\pi}\int_0^{2\pi} d\phi' \int_0^1 \frac{d\mu'}{\mu'} \int_{-\infty}^{\infty} dx' \\
&\quad \times \{S(\tau; \boldsymbol{x}_{\rm em}; x', \mu', \phi') R(\tau; x', \mu', \phi'; \boldsymbol{x}_{\rm in})\} \\
&\quad + \frac{1}{16\pi^2}\int_0^{2\pi} d\phi' \int_0^1 \frac{d\mu'}{\mu'} \int_{-\infty}^{\infty} dx' \\
&\int_0^{2\pi} d\phi'' \int_0^1 \frac{d\mu''}{\mu''} \int_{-\infty}^{\infty} dx'' \{S(\tau; \boldsymbol{x}_{\rm em}; x', \mu', \phi') \\
&\times R(\tau; x', -\mu', \phi'; x'', \mu'', \phi'') S(\tau; x'', \mu'', \phi''; \boldsymbol{x}_{\rm in})\}
\end{aligned} \tag{B1}$$

with

1. $\boldsymbol{x}_{\rm in} = (x_{\rm in}, \mu_{\rm in}, \phi_{\rm in})$, and $\boldsymbol{x}_{\rm em}$ is the corresponding vector for the emitted flux;
2. $x_{\rm in,em}$ are the incident and emitted frequencies;
3. $\mu_{\rm in,em} = \cos\theta_{\rm in,em}$ with incidence and emission angles $\theta_{\rm in,em}$;
4. $\phi_{\rm in,em}$ are the azimuthal incidence and emission angles;
5. τ—optical depth of the layer at the line center;
6. $\psi(x)$—line shape as a function of frequency;
7. S is the scattering function of the incident flux from ($x_{\rm in}$, $\mu_{\rm in}$, $\phi_{\rm in}$) to ($x_{\rm em}$, $\mu_{\rm em}$, $\phi_{\rm em}$) by the layer of thickness τ;
8. R is the angular dependent partial frequency redistribution function R_{II} from Hummer (1962).

Neglect the multiple scattering terms as we consider a thin layer and set

$$\eta = \frac{\psi(x_{\rm em})}{\mu_{\rm em}} + \frac{\psi(x_{\rm in})}{\mu_{\rm in}}. \tag{B2}$$

An integration factor of $\exp(\eta\tau)$ gives

$$\frac{\partial(S(\tau, x_{\rm em}, \mu_{\rm em}, \phi_{\rm em}, x_{\rm in}, \mu_{\rm in}, \phi_{\rm in})\exp(\eta\tau))}{\partial\tau} = R(\tau, x_{\rm em}, \mu_{\rm em}, x_{\rm in}, \mu_{\rm in})\exp(\eta\tau). \tag{B3}$$

Integrating from zero to optical depth τ and simplifying, we get

$$S(\tau; \boldsymbol{x}_{\rm em}; \boldsymbol{x}_{\rm in}) = \frac{R(\tau; \boldsymbol{x}_{\rm em}; \boldsymbol{x}_{\rm in})}{\eta}[1 - \exp(-\eta\tau)]. \tag{B4}$$

This is then expanded using a MacLaurin series and using $a = \eta\tau$ to get

$$S(\tau; \boldsymbol{x}_{\rm em}; \boldsymbol{x}_{\rm in}) = \frac{R(\tau; \boldsymbol{x}_{\rm em}; \boldsymbol{x}_{\rm in})\tau}{a}\sum_{n=1}^{\infty}\frac{(-a)^n}{n!}. \quad \text{(B5)}$$

Expanding this to the eighth order gives the thin layer approximation:

$$S(\tau; \boldsymbol{x}_{\rm em}; \boldsymbol{x}_{\rm in}) = R(\tau; \boldsymbol{x}_{\rm em}; \boldsymbol{x}_{\rm in})\tau\left(1 - a\left(1 - \frac{a}{2}\left(1 - \frac{a}{3}\left(1 - \frac{a}{4}\left(1 - \frac{a}{5}\left(1 - \frac{a}{6}\left(1 - \frac{a}{7}\left(1 - \frac{a}{8}\right)\right)\right)\right)\right)\right)\right)\right). \quad \text{(B6)}$$

For the thin layer transmission function, T, the equation of transfer is

$$\frac{\psi(x_{\rm in})}{\mu_{\rm in}}T(\tau; \boldsymbol{x}_{\rm em}; \boldsymbol{x}_{\rm in}) + \frac{\partial T(\tau; \boldsymbol{x}_{\rm em}; \boldsymbol{x}_{\rm in})}{\partial\tau} = \exp\left(-\tau\frac{\psi(x_{\rm em})}{\mu}\right)R(\boldsymbol{x}_{\rm em}; \boldsymbol{x}_{\rm in}) + ... \quad \text{(B7)}$$

Setting $\alpha = \frac{\psi(x_{\rm in})}{\mu_{\rm in}}$ and $\beta = \frac{\psi(x_{\rm em})}{\mu_{\rm em}}$ and using an integrating factor of $\exp(\alpha\tau)$ gives

$$T = R\frac{1}{\beta - \alpha}[\exp(-\alpha\tau) - \exp(-\beta\tau)] \quad \text{if} \quad \alpha \neq \beta. \quad \text{(B8)}$$

To get the thin layer approximation, expand both of the exponentials, and use $a = \alpha\tau$ and $b = \beta\tau$

$$T = R\tau(b - a)^{-1}\left[1 - a + \frac{a^2}{2!} - \frac{a^3}{3!} + \frac{a^4}{4!} + ... \right. \quad \text{(B9)}$$

$$\left. -1 + b - \frac{b^2}{2!} + \frac{b^3}{3!} - \frac{b^4}{4!} + ...\right]. \quad \text{(B10)}$$

Reorganizing these terms gives the expression

$$T = R\tau\left[c_1 - \frac{1}{2}\left(c_2 - \frac{1}{3}\left(c_3 - \frac{1}{4}\left(c_4 - \frac{1}{5}(c_5 - \frac{1}{6}\left(c_6 - \frac{1}{7}\left(c_7 - \frac{c_8}{8}\right)\right)\right)\right)\right)\right)\right], \quad \text{(B11)}$$

where

$$c_1 = 1 \quad \text{(B12)}$$

$$c_2 = a + b \quad \text{(B13)}$$

$$c_3 = a^2 + ab + b^2 \quad \text{(B14)}$$

$$c_4 = (a^2 + b^2) \times c_2 \quad \text{(B15)}$$

$$c_5 = a^4 + a^3b + b^2a^2 + ab^3 + b^4 \quad \text{(B16)}$$

$$c_6 = (a^3 + b^3) \times c_3 \quad \text{(B17)}$$

$$c_7 = a^6 + a^5b + a^4b^2 + a^3b^3 + b^2a^4 + ab^5 + b^6 \quad \text{(B18)}$$

$$c_8 = (a^4 + b^4) \times c_4. \quad \text{(B19)}$$

If $\alpha = \beta$, then the differential equation simplifies to

$$T = R\tau\exp(-\alpha\tau) = R\tau\exp(-a). \quad \text{(B20)}$$

Expanding this to the eighth order gives

$$L = -\frac{1}{2}\sum_n\left(\frac{(RV_i - \mathrm{RV}(\phi))^2}{\sigma^2} + \ln(\sigma^2)\right). \quad \text{(B21)}$$

Appendix C
Modeling IPH Brightnesses

Photons from IPH background enter the atmosphere from all directions. Consequently, we integrate over all incidence angles when computing the brightness of IPH scattered by Saturn's atmosphere, rather than the delta function in incidence angle used for the solar case. As outlined in Section 2.3.2, the IPH brightness is fit with respect to $\cos\theta_{\rm max}$, the angle to the direction of maximum brightness. At 9–10 au, the direction of maximum IPH brightness is closely aligned with the Sun direction.

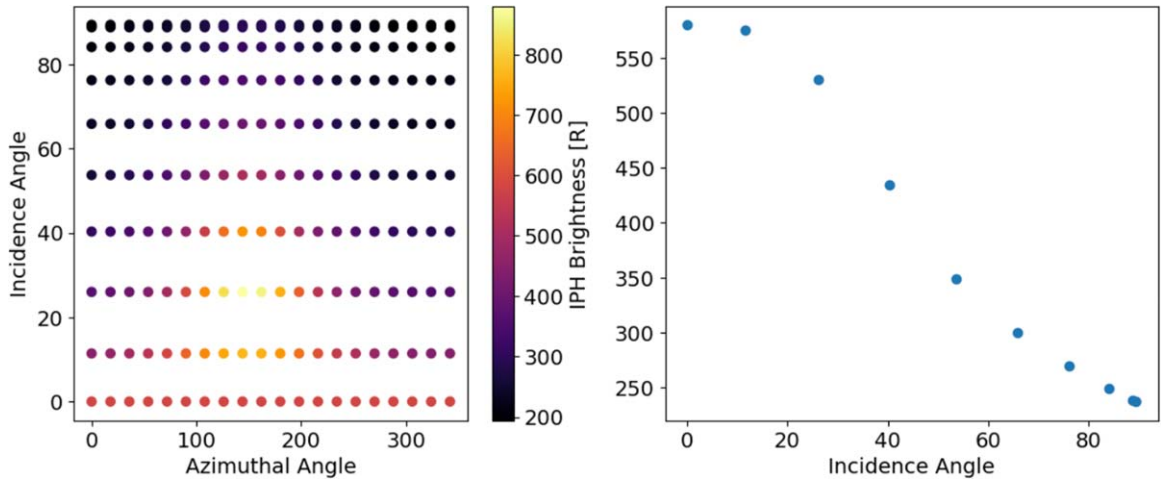

Figure 26. (a) Modeled IPH background brightness as a function of incidence and azimuthal angle for one observation pixel, using the fit in Figure 6. (b) Azimuthally averaged model IPH brightnesses, which are incorporated into the RT model in Equation (C1).

For each pixel, a grid of points is generated around the surface normal (see Figure 26), spanning both incidence angle and azimuthal direction. The angle of each point to the direction of maximum brightness is computed, and used to calculate the IPH brightness in that direction. This brightness of the IPH incident on the Saturn's atmosphere is scaled with the 28 day averaged solar flux at the time of observation. We use a Gaussian lineshape at a temperature of 16,000 K (Figure 4) in the radiative transfer model.

The scattered brightness from the scattered IPH Lymanα photons is given by

$$4\pi I_{\rm IPH}(\mu_{\rm em}) = \Delta\nu_{D,\rm Sat} \times 10^{-6} \int_0^{2\pi} d\phi_{\rm in} \times \int_0^1 d\mu_{\rm in} \int_{-\infty}^{\infty} dx_{\rm in} \int_{-\infty}^{\infty} dx_{\rm em} S(\tau; \boldsymbol{x}_{\rm em}; \boldsymbol{x}_{\rm in}) F_{\rm IPH}(\boldsymbol{x}_{\rm in}), \quad \text{(C1)}$$

where we have integrated over all incidence angles. The incident IPH flux is direction dependent such that

$$F_{\rm IPH}(\boldsymbol{x}_{\rm in}) = B_{\rm IPH}(\mu_{\rm in}, \phi_{\rm in}) \times f_{\rm IPH}(x_{\rm in}, \mu_{\rm in}, \phi_{\rm in}), \quad \text{(C2)}$$

where $f_{\rm IPH}(x_{\rm in}, \mu_{\rm in}, \phi_{\rm in})$ is the lineshape, which is normalized to 1. While this does not explicitly depend on the incidence angle, the direction of the normal vector relative to the sunward direction does impact the scattered IPH brightness.

We tested the impact of including a variable IPH Lyα lineshift and temperature into the radiative transfer model. We found that this resulted in scattered brightnesses varying by several Rayleighs ($\sim$5% of the IPH brightness), which in the context of Saturn is negligible and small compared to the observational uncertainties. Therefore, we simplify $f_{\rm IPH}(x_{\rm in}, \mu_{\rm in}, \phi_{\rm in}) = f_{\rm IPH}(x_{\rm in})$ in Equation C2.

Appendix D
Regression of the Lyα Brightnesses

As described in Section 2.2 and presented in Section 3.2, we have analyzed the extensive data set of Lyα emission brightnesses throughout the Cassini mission. In this section, we present supplementary material and figures from the regression analyses for the different mission periods.

Table 2
Coefficients for the Fit Used in the Multivariate Regression (See Equation (1)), for the 2004–2006 Observations

Variable	Coefficient	Mean Value	Confidence Interval
Constant	p_0	5.95×10^2	$(5.93 \times 10^2, 5.96 \times 10^2)$
$\theta_{\rm em}$	p_1	2.61×10^0	$(2.55 \times 10^0, 2.66 \times 10^0)$
$\theta_{\rm in}$	p_2	-8.85×10^0	$(-8.89 \times 10^0, -8.81 \times 10^0)$
$\phi_{\rm lat}$	p_3	1.26×10^0	$(1.15 \times 10^0, 1.37 \times 10^0)$
$\theta_{\rm em}^2$	p_4	9.28×10^{-2}	$(9.07 \times 10^{-2}, 9.50 \times 10^{-2})$
$\theta_{\rm em} \cdot \theta_{\rm in}$	p_5	7.08×10^{-3}	$(4.96 \times 10^{-3}, 9.19 \times 10^{-3})$
$\theta_{\rm in}^2$	p_6	-5.28×10^{-2}	$(-5.45 \times 10^{-2}, -5.11 \times 10^{-2})$
$\phi_{\rm lat}^2$	p_7	-1.35×10^{-2}	$(-1.61 \times 10^{-2}, -1.09 \times 10^{-2})$
$\phi_{\rm lat}^3$	p_8	-1.35×10^{-3}	$(-1.44 \times 10^{-3}, -1.25 \times 10^{-3})$

D.1. Northern Hemisphere Summer

For the northern hemisphere summer (here, taken as 2014–2017), the observed brightnesses show correlations with the emission angle, incidence angle, and latitude (see Figure 27). The comparison of the observed and predicted brightnesses for 2014–2017 is shown in Figure 12. We noted that the residuals in Figure 12(d) show quadratic behavior, being positive at small and large predicted brightnesses. However, the quadratic behavior seen in Figure 28(b) is not seen with respect to each independent variable (Figures 28(a)–(c)). Therefore, the choice of a combination of quadratic and cubic fits with respect to the independent variables (see Equation (1)) is sufficient to describe the brightnesses.

Figure 29 shows the fits of the multivariate regression in bins of latitude during the northern hemisphere summer. The variation of the observed brightness with incidence and emission angle is consistent across the full latitude range, and similar to the prediction of the radiative transfer model (see Figure 14(b)). The regions of difference with the radiative transfer model can be attributed to poor coverage in the latitude bin (see Figure 30), so the regression model is not well constrained.

D.2. Southern Hemisphere Summer

We apply the multivariate regression model (see Section 2.2) to the observations in the southern hemisphere summer (2004–2007). The fit coefficients are listed in Table 2.

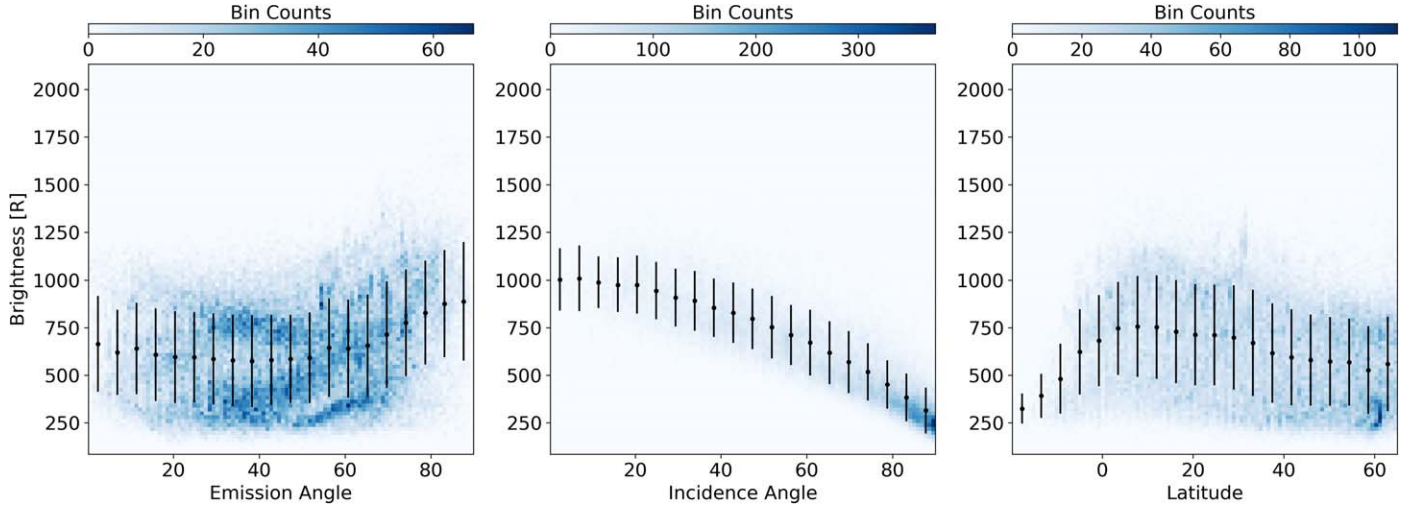

Figure 27. Brightness of the training data set in the late mission period (2014–2017; see Section 3.2) against emission angle, solar incidence angle, and latitude. The median and standard deviations of the observed brightnesses are given in bins of each independent variable.

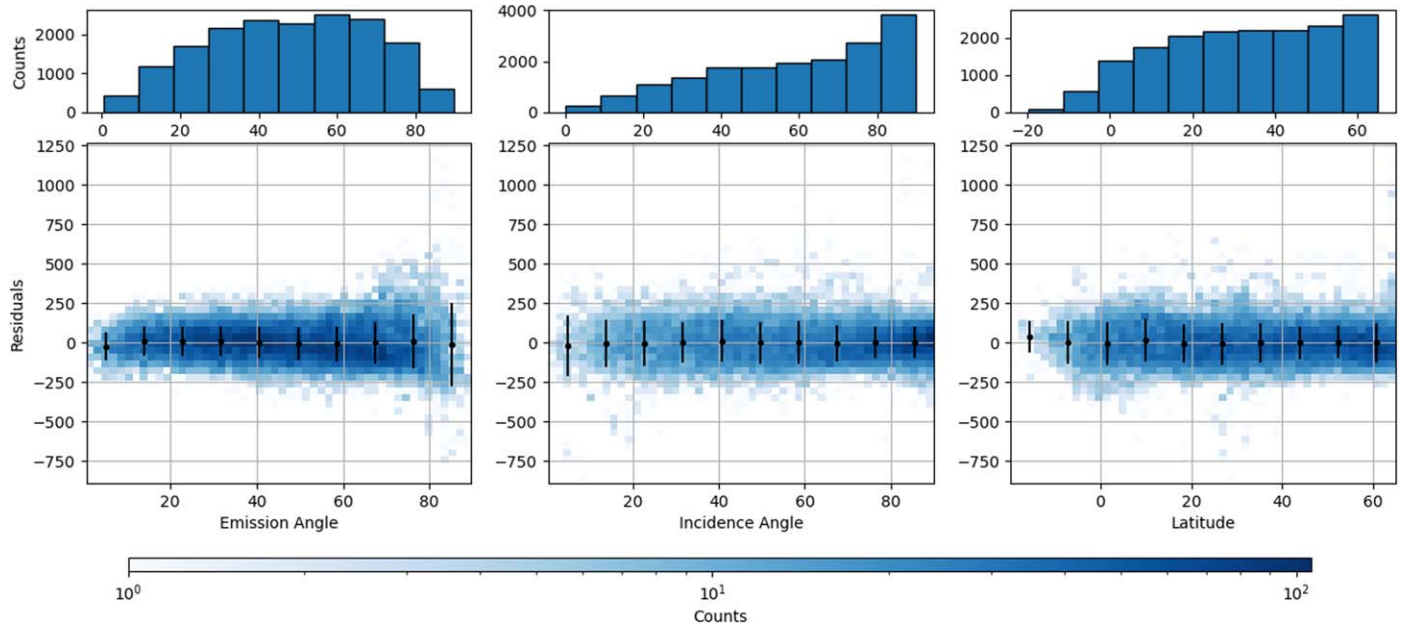

Figure 28. Residuals of the MVR analysis for the testing data set against each independent variable used in the model for the late mission period (2014–2017). The black points give the mean and standard deviations of the residual brightness.

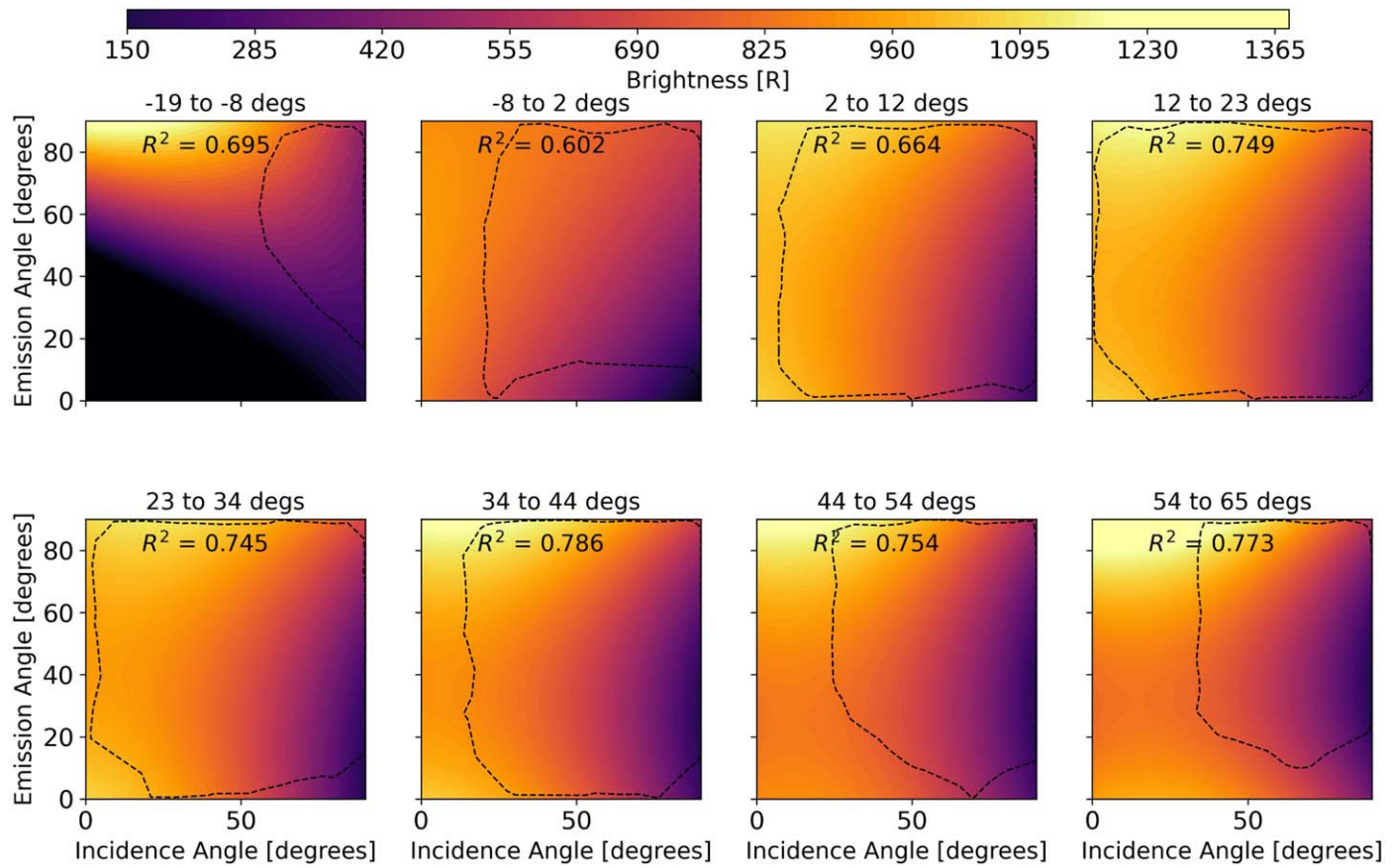

Figure 29. Predicted Lyα brightness vs. incidence and emission angles in bins of latitude during the northern hemisphere summer (2014–2017). The MVR analysis is applied using a quadratic expression in incidence and emission angles and is trained independently for each latitude bin. The observation coverages in the training data sets are shown in Figure 30.

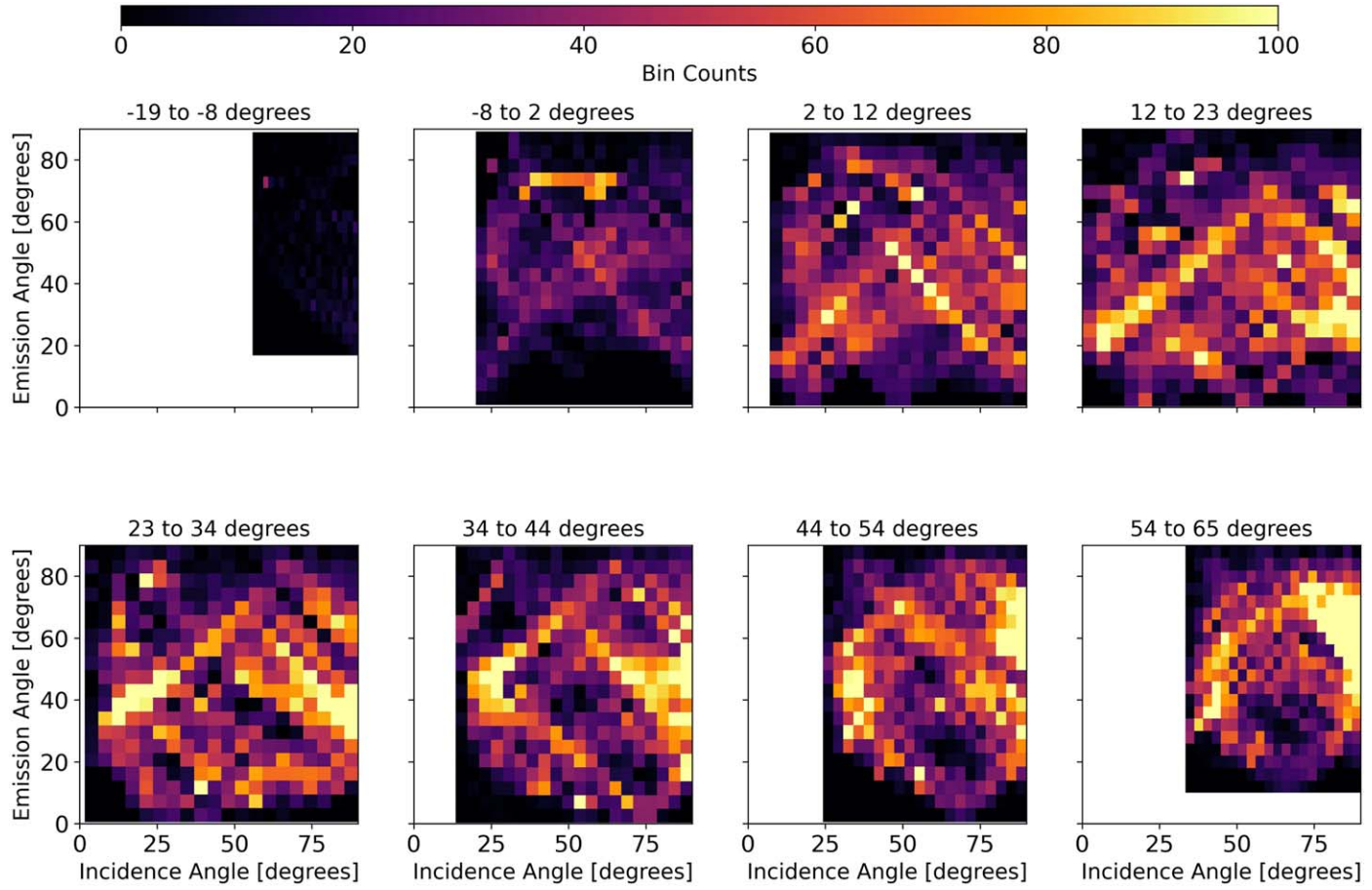

Figure 30. Counts of Lyα brightness observations vs. incidence and emission angles in bins of latitude during the northern hemisphere summer (2014–2017). The predicted brightnesses from each data set are shown in Figure 29.

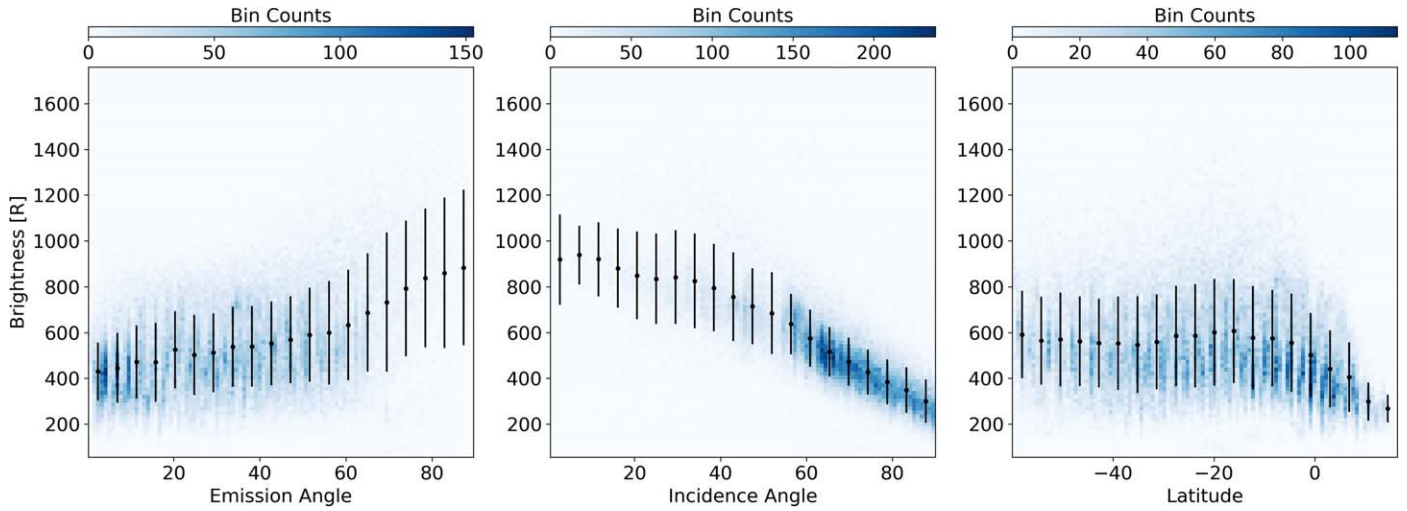

Figure 31. Brightness of the training data set in the southern hemisphere summer (2004–2007) against emission angle, solar incidence angle, and latitude. The median and standard deviations (black) of the observed brightnesses are given in bins of each independent variable.

Figure 31 shows the observed Lyα brightness during this period, showing similar behavior with incidence angle and emission angle to that observed in the northern hemisphere summer (see Figure 27). The dependence of the Lyα brightness on latitude has reversed, with a peak at -20° and a sharp decrease in brightness in the northern hemisphere. Figure 32 compares the observed brightnesses with predicted brightnesses and residuals. The model accurately reproduces the observed brightnesses between 200 R and 900 R, but overestimates some large brightnesses. There are few counts where the residuals are large, whereas the statistics are much stronger where the residuals are small (<200 R).

Similar to the northern summer, the quadratic nature of the residuals in Figure 32(b) is not replicated in the dependences

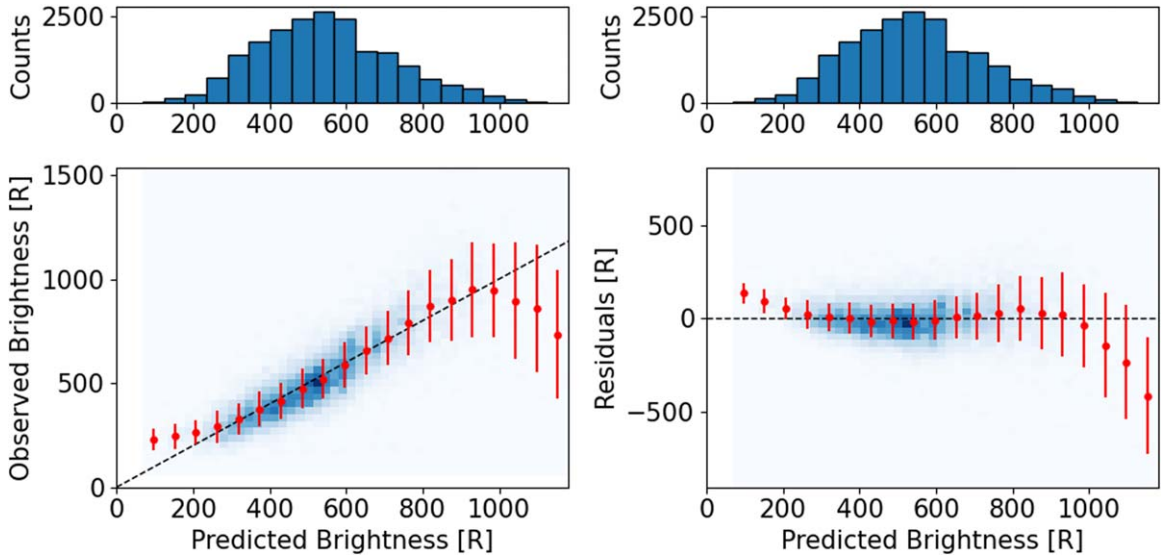

Figure 32. (a), (b) Testing data counts vs. predicted brightness from the MVR for 2004–2007. (c) Observed brightnesses and (d) residuals vs. predicted brightnesses for the testing data set (blue) with the averages and standard deviations shown in red.

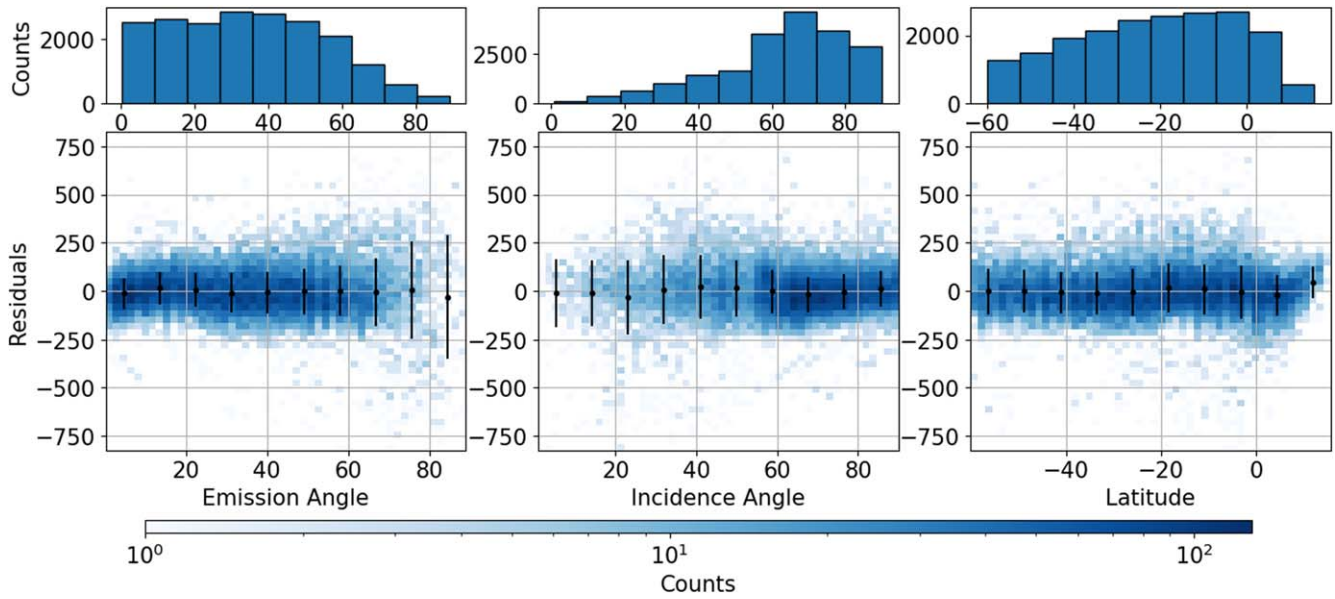

Figure 33. Residuals of the MVR analysis for the testing data set for 2004–2007 against each independent variable used in the model. The black points give the mean and standard deviations of the residual brightness.

on each independent variable (see Figure 33). The residuals show little dependence on each of the independent variables, suggesting higher order terms are not required to improve the fits.

The dependence of the predicted brightness on the incidence and emission angles at $\phi_{\rm lat} = -20^{\circ}$ (see Figure 34) is very similar to that seen in the northern hemisphere summer, and to the predictions of the radiative transfer model (see Figure 14).

The same structure in the predicted brightness is retrieved for each latitude bin with a good fit ($R^2 > 0.6$, Figure 35) for all bins in the southern hemisphere, where more observations were available (see Figure 36). Some bins, such as $\phi_{\rm lat} = [-60, -49]$, predict large brightnesses at low emission angles, contrary to the radiative transfer model. In each of these cases, the data coverage does not extend to low emission angles, so this should not be interpreted physically.

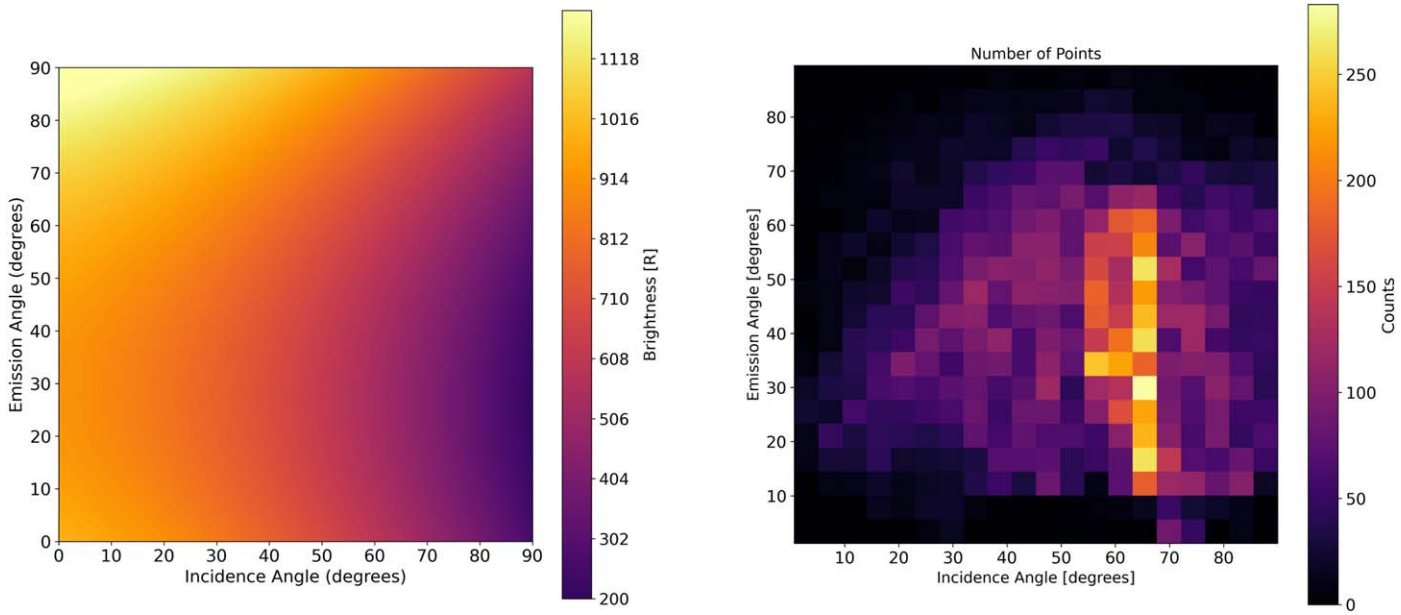

Figure 34. (Left) Predicted brightness as a function of solar incidence and emission angles from the MVR analysis at a latitude of −20°N for the 2004–2007 data set. (Right) Observation counts as a function of solar incidence and emission angles used to train the MVR analysis for the 2004–2007 data set.

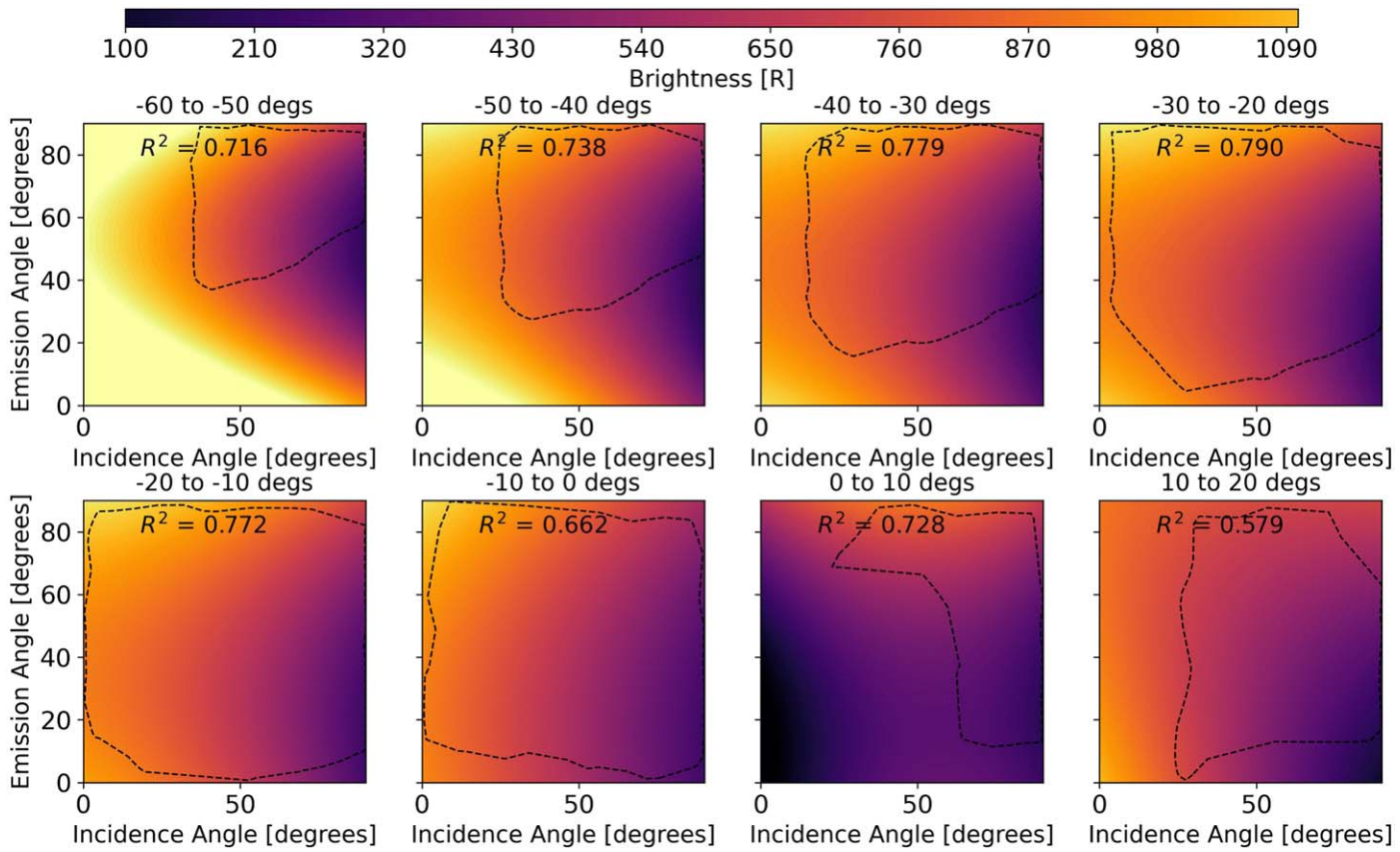

Figure 35. Predicted Lyα brightness vs. incidence and emission angles in bins of latitude during the southern hemisphere summer (2004–2007). The MVR analysis is applied using a quadratic expression in incidence and emission angles and is trained independently for each latitude bin. The observation coverage in the training data set is shown in Figure 36.

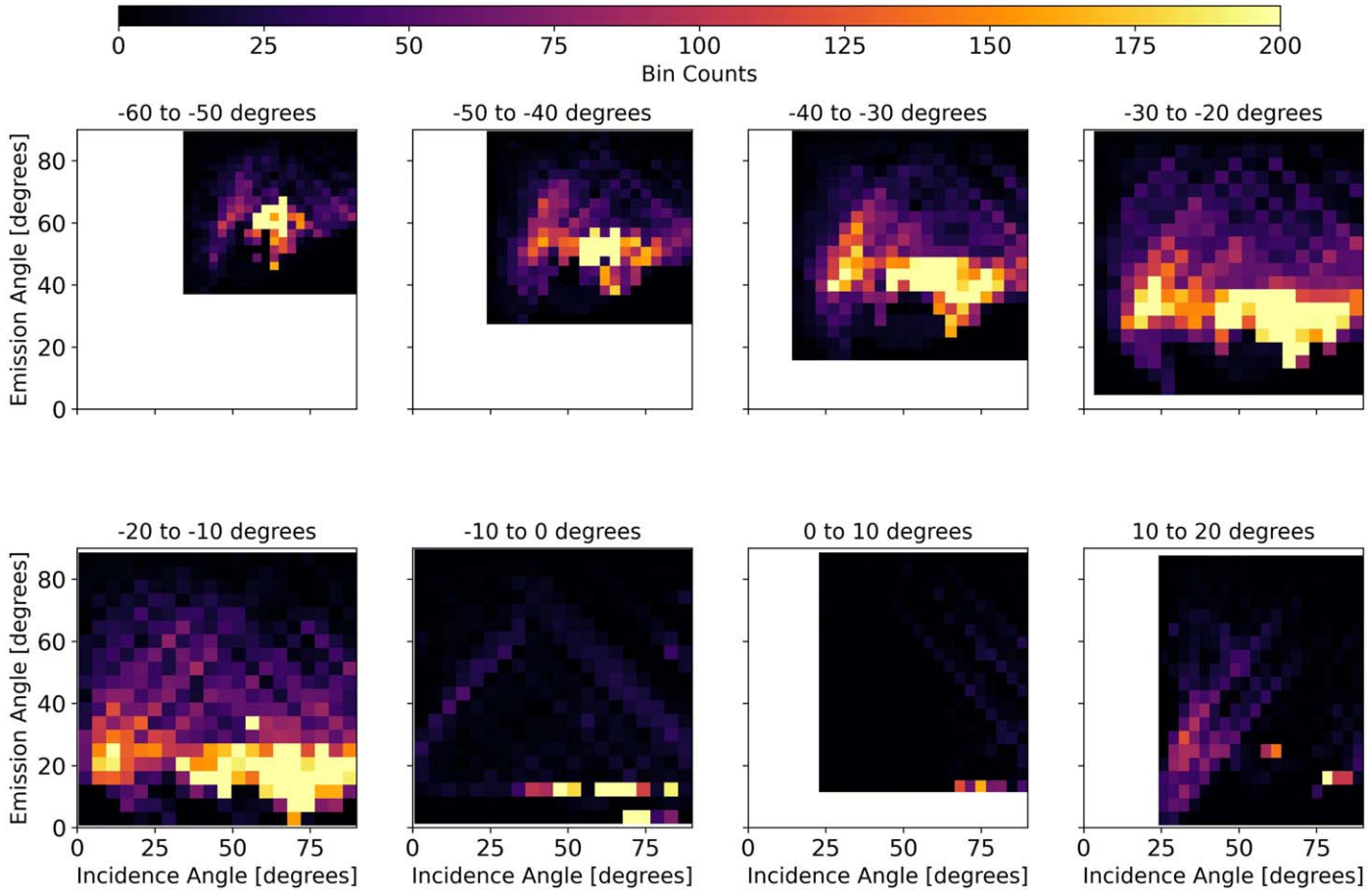

Figure 36. Counts of Lyα brightness observations vs. incidence and emission angles in bins of latitude during the southern hemisphere summer (2004–2007). The predicted brightnesses from each data set are shown in Figure 35.

Appendix E
Absorption by the Interplanetary Lyα

Between 1 au, where the Lyα profile has been measured (Lemaire et al. 2005), and Saturn, IPH background absorbs some of the Lyα, particularly near the line center, reducing the line-center flux by up to 13%. As the flux at line center is important for resonance scattering, we model the absorption of the IPH background using the IPH model of Quémerais et al. (2013a), Izmodenov et al. (2013), which is discussed in Section 2.3.2.

We calculate the absorption for 36 radial profiles distributed along Saturn's orbit, relative to the flow of LISM. The optical depth of the IPH background is integrated radially to a heliocentric distance of 9.5 au, including the Doppler shift and width of the absorption profile resulting from the bulk IPH velocity.

Using the optical depth, we correct the Lyα lineshape and average the absorption profiles around the line center. It is assumed that resonance scattering is symmetric about the line center in the radiative transfer model, so the absorption must also be made symmetric.

Figure 4 shows the corrected Lyα lineshape for the mean absorption profile (dashed black line) with the absorption variability (black shaded region), compared to the flux shape without IPH absorption.

Appendix F
IPH Observations

The observations of the Lyα IPH background we use in Section 3.1 are listed in Table 3.

Table 3
Observations of the IPH Lyα Background by Cassini/UVIS in 2006, with Heliocentric Distance (D_H) and Background Brightness

Day of Year	Lead	D_H	Background (R)	Lyα (R)	Scaled B (R)	R.A.	Decl.	R.A.$_\odot$	Decl.$_\odot$
014	CIRS	9.08	4.04 ± 2.20	251 ± 72	229 ± 65	101.7	−2.75	309.91	−19.04
015	UVIS	9.08	5.50 ± 1.10	557 ± 61	508 ± 55	279.1	3.01	309.92	−19.02
	ISS	9.08	5.74 ± 0.69	596 ± 39	544 ± 35	277.4	3.18	309.93	−19.02
	CIRS	9.08	5.80 ± 0.94	348 ± 47	317 ± 42	101.7	−2.75	309.91	−19.03
	CIRS	9.08	5.75 ± 1.66	202 ± 14	184 ± 12	101.2	−2.81	309.92	−19.03
057	VIMS	9.10	5.53 ± 1.22	183 ± 12	172 ± 11	134.2	0.75	311.46	−18.67
058	UVIS	9.10	5.45 ± 1.67	619 ± 52	582 ± 48	309.6	−0.24	311.53	−18.65
	CIRS	9.10	5.40 ± 0.64	673 ± 45	633 ± 42	309.0	−0.17	311.54	−18.65
	ISS	9.10	5.91 ± 1.04	286 ± 74	269 ± 69	133.2	0.64	311.49	−18.66
077	CIRS	9.10	5.47 ± 1.44	304 ± 27	288 ± 25	73.5	−5.12	312.28	−18.52
	ISS	9.10	6.24 ± 2.71	341 ± 36	323 ± 34	72.2	−5.2	312.29	−18.52
078	CIRS	9.09	5.46 ± 1.70	433 ± 32	411 ± 30	248.8	5.42	312.30	−18.51
	VIMS	9.09	4.97 ± 1.51	444 ± 15	421 ± 14	249.5	5.38	312.30	−18.51
121	UVIS	9.11	5.66 ± 1.33	596 ± 55	546 ± 50	282.1	2.72	313.84	−18.12
140	UVIS	9.11	5.27 ± 1.54	274 ± 37	250 ± 33	44.0	−6.31	314.62	−17.97
183	UVIS	9.12	5.78 ± 1.15	445 ± 28	416 ± 26	255.3	4.92	316.14	−17.58
250	CIRS	9.14	5.44 ± 0.92	333 ± 21	310 ± 19	19.2	−15.1	318.67	−16.97
	UVIS	9.14	4.85 ± 2.06	330 ± 27	307 ± 25	20.6	−15.8	318.67	−16.96
	CIRS	9.14	5.52 ± 1.15	247 ± 84	229 ± 78	25.9	−18.0	318.68	−16.96
	ISS	9.14	6.08 ± 1.12	249 ± 43	231 ± 40	204.7	17.6	318.69	−16.96
	ISS	9.14	5.51 ± 1.37	237 ± 52	220 ± 48	205.3	17.8	318.67	−16.96
266	UVIS	9.14	5.10 ± 0.94	288 ± 38	267 ± 35	27.2	−20.6	319.26	−16.81
282	CIRS	9.14	4.73 ± 1.79	300 ± 8	279 ± 7	28.5	−28.5	319.84	−16.66
	CIRS	9.14	5.40 ± 1.01	337 ± 15	313 ± 13	210.2	33.8	319.86	−16.66
283	CIRS	9.14	5.01 ± 1.12	292 ± 17	271 ± 15	208.0	32.3	319.89	−16.64
297	UVIS	9.15	5.43 ± 0.88	317 ± 11	298 ± 10	31.0	−35.3	320.40	−16.52
299	VIMS	9.15	5.73 ± 1.55	315 ± 31	296 ± 29	219.4	36.3	320.44	−16.50
346	UVIS	9.16	5.00 ± 1.18	293 ± 33	271 ± 30	39.6	−38.7	322.15	−16.04
	CIRS	9.16	5.10 ± 2.15	289 ± 28	267 ± 25	215.1	42.9	322.18	−16.02
361	CIRS	9.16	5.37 ± 1.01	308 ± 12	288 ± 11	34.8	−44.6	322.72	−15.88
362	CIRS	9.16	5.21 ± 0.51	300 ± 25	281 ± 23	218.3	48.5	322.74	−15.87
	CIRS	9.16	5.21 ± 0.84	286 ± 22	268 ± 20	219.2	49.6	322.75	−15.87

Note. The R.A. and decl. of the observation and the sunward direction ($\odot$) are given. Lead instruments for the observations include the Cassini Imaging Science Subsystem (ISS; Porco et al 2004).

ORCID iDs

P. Stephenson https://orcid.org/0000-0002-1753-5269
T. T. Koskinen https://orcid.org/0000-0003-3071-8358
J. I. Moses https://orcid.org/0000-0002-8837-0035

References

Atreya, S., Waite, J., Jr, Donahue, T., Nagy, A., & McConnell, J. C. 1984, Saturn (Tucson, AZ: Univ. of Arizona Press), 239
Atreya, S. K. 1982, P&SS, 30, 849
Barker, E., Cazes, S., Emerich, C., et al. 1980, ApJ, 242, 383
Barth, C. A., Rusch, D. W., Thomas, R. J., et al. 1983, GeoRL, 10, 237
Ben-Jaffel, L., Moses, J. I., West, R. A., et al. 2023, PSJ, 4, 54
Ben-Jaffel, L., Prangé, R., Sandel, B. R., et al. 1995, Icar, 113, 91
Broadfoot, A. L., Sandel, B. R., Shemansky, D. E., et al. 1981, Sci, 212, 206
Brown, Z., Koskinen, T., Müller-Wodarg, I., et al. 2020, NatAs, 4, 872
Brown, Z. L., Koskinen, T. T., Moses, J., & Guerlet, S. 2024, Icar, 417, 116133
Brown, Z. L., Medvedev, A. S., Starichenko, E. D., Koskinen, T. T., & Müller-Wodarg, I. C. 2022, GeoRL, 49, e2021GL097219
Bzowski, M., Möbius, E., Tarnopolski, S., Izmodenov, V., & Gloeckler, G. 2009, SSRv, 143, 177
Chen, F. Z., & Wu, C. Y. 2004, JQSRT, 85, 195
Clarke, J. T., Moos, H. W., Atreya, S. K., & Lane, A. L. 1981, Natur, 290, 226
Dessler, A. J., Sandel, B. R., & Atreya, S. K. 1981, P&SS, 29, 215
Dialynas, K., Krimigis, S. M., Decker, R. B., & Mitchell, D. G. 2019, GeoRL, 46, 7911
Emerich, C., Ben Jaffel, L., & Prangé, R. 1993, P&SS, 41, 363
Esposito, L. W., Barth, C. A., Colwell, J. E., et al. 2005, SSRv, 115, 299
Flasar, F. M., Kunde, V. G., Abbas, M. M., et al. 2005, SSRv, 115, 169
Gladstone, G. R., Pryor, W. R., Hall, D. T., et al. 2021, AJ, 162, 241
Gladstone, G. R., Pryor, W. R., Stern, S. A., et al. 2018, GeoRL, 45, 8022
Guerlet, S., Fouchet, T., Spiga, A., et al. 2018, JGRE, 123, 246
Gustin, J., Stewart, I., Gérard, J. C., & Esposito, L. 2010, Icar, 210, 270
Hinteregger, H. E., Fukui, K., & Gilson, B. R. 1981, GeoRL, 8, 1147
Hue, V., Cavalié, T., Dobrijevic, M., Hersant, F., & Greathouse, T. K. 2015, Icar, 257, 163
Hue, V., Greathouse, T. K., Cavalié, T., Dobrijevic, M., & Hersant, F. 2016, Icar, 267, 334
Hummer, D. G. 1962, MNRAS, 125, 21
Izmodenov, V. V., & Alexashov, D. B. 2020, A&A, 633, L12
Izmodenov, V. V., Gruntman, M., & Malama, Y. G. 2001, JGRA, 106, 10681
Izmodenov, V. V., Katushkina, O. A., Quémerais, E., & Bzowski, M. 2013, Cross-Calibration of Far UV Spectra of Solar System Objects and the Heliosphere (Berlin: Springer), 2
Katushkina, O. A., Quémerais, E., Izmodenov, V. V., Alexashov, D. B., & Sandel, B. R. 2016, JGRA, 121, 93
Katushkina, O. A., Quémerais, E., Izmodenov, V. V., Lallement, R., & Sandel, B. R. 2017, JGRA, 122, 921
Koskinen, T. T., & Guerlet, S. 2018, Icar, 307, 161
Koskinen, T. T., Moses, J. I., West, R. A., Guerlet, S., & Jouchoux, A. 2016, GeoRL, 43, 7895
Koskinen, T. T., Sandel, B. R., Yelle, R. V., Holsclaw, G. M., & Quemerais, E. 2020, Icar, 339, 113594
Koskinen, T. T., Sandel, B. R., Yelle, R. V., et al. 2013, Icar, 226, 1318
Koskinen, T. T., Sandel, B. R., Yelle, R. V., et al. 2015, Icar, 260, 174
Koskinen, T. T., Strobel, D. F., & Brown, Z. 2021, Icar, 362, 114396
Krstić, P. S., & Schultz, D. R. 1999, PhRvA, 60, 2118
Larsson, M., McCall, B. J., & Orel, A. E. 2008, CPL, 462, 145

Lemaire, P., Emerich, C., Vial, J. C., et al. 2005, AdSpR, 35, 384
Machol, J., Snow, M., Woodraska, D., et al. 2019, E&SS, 6, 2263
Matson, D. L., Spilker, L. J., & Lebreton, J. P. 2002, SSRv, 104, 1
McClintock, W. E., Snow, M., & Woods, T. N. 2005, The Solar Radiation and Climate Experiment (SORCE): Mission Description and Early Results (Berlin: Springer), 259
McGrath, M. A., & Clarke, J. T. 1992, JGRA, 97, 13691
Mitchell, D. G., Kurth, W. S., Hospodarsky, G. B., et al. 2009, JGRA, 114, A02212
Moses, J. I., & Bass, S. F. 2000, JGRE, 105, 7013
Moses, J. I., Bézard, B., Lellouch, E., et al. 2000a, Icar, 143, 244
Moses, J. I., Brown, Z. L., Koskinen, T. T., et al. 2023, Icar, 391, 115328
Moses, J. I., & Greathouse, T. K. 2005, JGRE, 110, 1
Moses, J. I., Lellouch, E., Bézard, B., et al. 2000b, Icar, 145, 166
Müller-Wodarg, I. C., Koskinen, T. T., Moore, L., et al. 2019, GeoRL, 46, 2372
O'Donoghue, J., Moore, L., Connerney, J., et al. 2019, Icar, 322, 251
Porco, C. C., West, R. A., Squyres, S., et al. 2004, SSRv, 115, 363
Pryor, W. R., Gladstone, G. R., Retherford, K. D., & Tobiska, W. K. 2022, AJ, 164, 46
Pryor, W. R., Gladstone, G. R., Retherford, K. D., et al. 2024, ApJ, 960, 117
Quémerais, E. 2000, A&A, 358, 353
Quémerais, E., Bertaux, J. L., Lallement, R., Sandel, B. R., & Izmodenov, V. 2003, JGRE, 108, 8029
Quémerais, E., Chaufray, J. Y., Koutroumpa, D., et al. 2020, SSRv, 216, 1
Quémerais, E., & Izmodenov, V. 2002, A&A, 396, 269
Quémerais, E., Lallement, R., Ferron, S., et al. 2006, JGRA, 111, A09114
Quémerais, E., Sandel, B. R., Izmodenov, V. V., & Gladstone, G. R. 2013, Cross-Calibration of Far UV Spectra of Solar System Objects and the Heliosphere (Berlin: Springer), 141
Sandel, B. R., Shemansky, D. E., Broadfoot, A. L., et al. 1982, Sci, 215, 548
Serigano, J., Hörst, S. M., He, C., et al. 2020, JGRE, 125, e2020JE006427
Serigano, J., Hörst, S. M., He, C., et al. 2022, JGRE, 127, e2022JE007238
Shemansky, D. E., & Liu, X. 2012, CaJPh, 90, 817
Shemansky, D. E., Liu, X., & Melin, H. 2009, P&SS, 57, 1659
Skinner, T. E., DeLand, M. T., Ballester, G. E., et al. 1988, JGRA, 93, 29
Swaczyna, P., McComas, D. J., Zirnstein, E. J., et al. 2020, ApJ, 903, 48
Waite, J. H., Cravens, T. E., Kozyra, J., et al. 1983, JGRA, 88, 6143
Waite, J. H., Perryman, R. S., Perry, M. E., et al. 2018, Sci, 362, eaat2382
Wallace, L., Yelle, R. V., Wallace, L., & Yelle, R. V. 1989, ApJ, 346, 489
Weiser, H., Vitz, R. C., & Moos, H. W. 1977, Sci, 197, 755
Woods, T. N., Tobiska, W. K., Rottman, G. J., & Worden, J. R. 2000, JGRA, 105, 27195
Yelle, R. V. 1988, ApJ, 332, 514
Yelle, R. V., Sandel, B. R., Shemansky, D. E., & Kumar, S. 1986, JGRA, 91, 8756
Yelle, R. V., Serigano, J., Koskinen, T. T., et al. 2018, GeoRL, 45, 951
Yelle, R. V., & Wallace, L. 1989, ApJ, 346, 481
Yelle, R. V., Wallace, L., Yelle, R. V., & Wallace, L. 1989, ApJ, 346, 481